

論文 / 著書情報  
Article / Book Information

論題(和文)	
Title(English)	High-mobility two-dimensional electron gas in polar oxide interfaces
著者(和文)	大友 明
Authors(English)	Akira Ohtomo
出典(和文)	2009 WPI-AIMR Annual Workshop アブストラクト集, , ,
Citation(English)	2009 WPI-AIMR Annual Workshop Abstract, , ,
発行日 / Pub. date	2009, 3

# Surface and interface engineering of ZnO based heterostructures

A. Ohtomo<sup>1\*</sup>, A. Tsukazaki<sup>1,2</sup>, Kawasaki<sup>1,3,4</sup>

<sup>1</sup> *Institute for Materials Research, Tohoku University, Sendai 980-8577, Japan.*

<sup>2</sup> *PRESTO, Japan Science and Technology Agency, Tokyo 102-0075, Japan.*

<sup>3</sup> *WPI Advanced Institute for Materials Research, Tohoku University, Sendai 980-8577, Japan.*

<sup>4</sup> *CREST, Japan Science and Technology Agency, Tokyo 102-0075, Japan.*

\* Electronic mail: aohtomo@imr.tohoku.ac.jp

ZnO and related alloys are an important class of materials towards realizing transparent electronics because of their natures of wide band-gap and high mobility as well as practical advantages such as available *p*-type materials and bulk single crystals, low-cost production, and absence of toxicity. Our studies for 10 years have enabled surface and interface engineering in an atomic scale, presenting a promising technologies for developing various kinds of electrical devices. Quality of the epitaxial films was drastically improved when grown on high-temperature annealed buffer layers prepared on lattice-matched ScAlMgO<sub>4</sub> substrates by using pulsed-laser deposition. We carefully investigated growth temperature dependences of surface morphology and electrical properties. As the result, electron mobility was recorded to be 440 cm<sup>2</sup>/Vs at room temperature and 5500 cm<sup>2</sup>/Vs at 1 K, leading to recent observation of quantum Hall-effect (QHE) in abrupt ZnO/Mg<sub>x</sub>Zn<sub>1-x</sub>O interfaces. Two-dimensional electron gas was spontaneously formed in the interface due to the polarization mismatch between the layers. The observation of QHE allows to access direct determination of the interfacial electronic structure. In addition, field-effect control of 2DEG has been demonstrated by the use of lattice-matched interfaces as high-mobility channels.

Keywords: ZnO, surface, interface, epitaxial growth, pulsed-laser deposition, quantum Hall-effect, field-effect transistor

## I. INTRODUCTION

### A. Surface transport of ZnO

ZnO is the only example of the class II-VI semiconductors for which surface transport has been intensively examined.<sup>1</sup> Most of the previous studies were performed in a period from 1970's to 1980's. The particular interest was relevance to two-dimensional electron gas (2DEG) in clean semiconductor heterostructures, Si/SiO<sub>2</sub> and GaAs/AlGaAs for examples, which were also actively studied in those days. In contrast to these cubic semiconductors, ZnO has hexagonal wurtzite structure, in which Zn and O ions alternately stack along the *c*-axis direction, giving rise to polar (0001) and (000-1) surfaces (also expressed Zn-face and O-face, respectively). Chemical and physical properties of these surfaces are known to be different, which have also been found for their surface transport behaviors. Eger *et al.* reported surface electrons with density in excess of  $1 \times 10^{14} \text{ cm}^{-2}$  could be accumulated in the O-face of a semi-insulating single crystal by applying current pulses through an electrolyte.<sup>2</sup> Their numerical analysis suggested that accumulated electrons were confined within a few unit cells from the surface and accordingly quantized in discrete energy levels. Goldstein *et al.* measured temperature dependence of surface conductivity for strong accumulation layers induced by exposure to thermalized He<sup>+</sup> ion.<sup>3</sup> Similar results were obtained for a vacuum-cleaved surface exposed to atomic hydrogens.<sup>4</sup>

In any cases, metallic conductivity was observed at electron density higher than mid  $10^{13} \text{ cm}^{-2}$ . Peak value of Hall mobility for the O-face was found to be  $\sim 100 \text{ cm}^2/\text{Vs}$  at room temperature and less than  $200 \text{ cm}^2/\text{Vs}$  at low temperatures. The Zn-face was found to be chemically unstable and the mobility was much lower in the whole range of temperature and electron density. Compared to bulk mobility, these values were only a half at room temperature and an order magnitude lower at low temperatures. To account for this behavior, it was believed that surface roughness and disorder originated from polishing or cleaving caused carrier scattering. Although recent technological advances in the growth of high-quality single-crystal and in preparation of atomically flat surface should have reduced their influences, quantized effect in surface transport has not been observed before our studies.

### B. Quantum Hall effect in semiconductor heterostructures

Certain aspects of 2DEG behavior in semiconductor heterostructures have been studied by observing the quantum Hall effect (QHE)— a quantized magnetotransport accompanied with Shubnikov-de Haas (SdH) oscillations in the longitudinal resistivity  $\rho_{xx}$  and Landau plateaus in the Hall resistivity  $\rho_{xy}$ . High-precision measurement revealed that  $\rho_{xy}$  at particular carrier densities has fixed values, given by  $h/e^2i$  ( $i = 1, 2,$

3, ..) =  $25,813/i \Omega$ , where  $h$  is Plank's constant and  $e$  is the charge of the electron.<sup>5</sup> Early results were obtained in the  $p$ -channel Si MOSFETs (metal-oxide-semiconductor field-effect transistor), where 2DEG are formed in  $n$ -type surface inversion layer by applying positive gate electric field. Hall mobility of the inversion layer is a few times 10000  $\text{cm}^2/\text{Vs}$  at low temperature. Much higher mobility ( $> 10^7 \text{ cm}^2/\text{Vs}$ ) was achieved for the 2DEG in GaAs/AlGaAs interface as molecular-beam epitaxy (MBE) technology was matured for the growth of modulation doped structures. To date, the electronic properties of 2DEG are well characterized for a number of III-V semiconductors and they are now providing ideal and commercially available systems for studying mesoscopic to nano-scale science.

Table I presents comparisons of some materials properties among the semiconductor heterostructures, in which quantum Hall-effect has been observed.<sup>6-12</sup> The observation of SdH oscillations requires conditions such as  $\omega_c \tau > 1$  and  $\hbar \omega_c > k_B T$ , where  $\omega_c$  is the cyclotron frequency and  $\tau$  is the carrier relaxation time. The first relation simply means that applying magnetic field in excess of 1 T is necessary to let them emerge in a system having mobility of  $\sim 10000 \text{ cm}^2/\text{Vs}$ . Mobility ( $\mu$ , drift mobility) is defined by  $\mu = e\tau/m^*$ , where  $m^*$  is effective mass of charge carriers, therefore for a measured constant of  $\mu$ ,  $\tau$  is longer in materials having heavier  $m^*$ .  $\tau$  is extremely sensitive to the defect density and temperature dependent scattering origins. Given the fixed defect density and measurement temperature, it depends on difference in electronegativity of constituent atoms— the shorter  $\tau$  becomes, the stronger ionic bonding contributes. There is a similar tendency for  $m^*$ , but its change with increasing the electronegativity factor is opposite to  $\tau$ . Taken together, enhancement of mobility in ionic semiconductors is more challenging subject for observing quantized surface transport phenomena. Thus, development of epitaxial growth technology of oxide heterostructures is very important.

There are a few examples of oxide heterostructures that satisfy aforementioned conditions for the observation of SdH oscillations, one of which is a charge transfer interface of (100)  $\text{LaAlO}_3/\text{SrTiO}_3$ .<sup>13</sup> In this particular system, coulomb screening is sufficiently large to yield mobility as high as  $\sim 10000 \text{ cm}^2/\text{Vs}$  at low temperatures because of extremely high dielectric constant of  $\text{SrTiO}_3$ . It undergoes a metal-to-insulator transition (MIT) at critical carrier density of  $10^{14} \text{ cm}^{-2}$ , two to three orders of magnitude higher than a range required for the observation of QHE. This situation is similar to the surface transport in ZnO and for both cases critical carrier density must be reduced below  $10^{12} \text{ cm}^{-2}$  for the observation of QHE. Thus, again one has to develop a suitable growth method for making high-quality epitaxial films.

### C. Mobility of ZnO

Intrinsic mobility of ZnO single crystal is known to be the highest (230 cm<sup>2</sup>/Vs and 2200 cm<sup>2</sup>/Vs at room temperature and 50 K, respectively) among wide band-gap oxide semiconductors.<sup>14</sup> For fundamental research that we describe here, it is necessary to eliminate defects and impurities in epitaxial films that can serve as severe scattering centers. On the other hand, a range of mobility required for a thin-film transistor (TFT) driving a flat-panel display (LCD) is 1 to 10 cm<sup>2</sup>/Vs, easily achievable even in a polycrystalline film deposited on a glass substrate.

Figures 1(a)-(c) illustrate prototype transistor structures that we have fabricated by using various materials to be integrated with ZnO. The first device was actually based on polycrystalline film deposited on a bottom gate glass substrate [Fig. 1(a)].<sup>15</sup> The majority of the devices reported by others has similar bottom gate structure, but we employed the same stagger type device design and the same materials set used in the practical devices for commercial LCD, except for the amorphous Si (a-Si) channel layer that is replaced by ZnO combined with CaHfO<sub>x</sub> buffer layer. Typical field-effect mobility ( $\mu_{FE}$ ) was 7 cm<sup>2</sup>/Vs for our TFTs fabricated at 300°C, a standard process temperature used for making a-Si-TFT. Although the obtained mobility was higher than that for a-Si TFT (~0.5 cm<sup>2</sup>/Vs), further enhancement of  $\mu_{FE}$  in the polycrystalline ZnO TFT was found to be difficult due to a severe influence of high-density grain boundaries to the carrier scattering.<sup>16</sup> On the other hand, a top-gate FET based on a single-crystalline film epitaxially grown on a lattice-matched substrate channels exhibited reasonably high  $\mu_{FE}$  (40 cm<sup>2</sup>/Vs) [Fig. 1(b)].<sup>17</sup> Further enhancement of  $\mu_{FE}$  was feasible when we employed Mg<sub>1-x</sub>Ca<sub>x</sub>O layers as a lattice-matched gate dielectric.<sup>18</sup> The extracted  $\mu_{FE}$  was as high as 250 cm<sup>2</sup>/Vs,<sup>19</sup> in particular the highest among wide band-gap oxide semiconductor based devices ever reported. These progresses are summarized in Fig. 1(d).

Hall mobility of the epitaxial films has also been increased over the years as defect density is reduced by developments of various epitaxial growth techniques. A value higher than bulk single crystals (300 cm<sup>2</sup>/Vs) was recorded by inserting high-temperature annealed buffer layer between the substrate and the ZnO film, as shown in Fig. 1(c). Having established this level of epitaxial film quality, we were able to make nitrogen-doped *p*-type films by using repeated temperature modulation epitaxy technique.<sup>20</sup> Systematic studies for optimizing growth conditions yielded Hall mobility as high as 440 cm<sup>2</sup>/Vs,<sup>21</sup> leading to the first successful observation of quantum Hall effect in oxides.<sup>12</sup> Therefore, a fundamental technology level have already been achieved for realizing transparent electronics, possibly altering some functions of current practical devices.<sup>22</sup> Very recently, we have achieved Hall mobility in excess of

20,000 cm<sup>2</sup>/Vs at 2 K, which is comparable to that for the Si MOSFET, presenting a promising possibility for realizing oxide electronics.

In this article, we first describe advantages of lattice-matched substrates to make atomically regulated surface and interface, followed by experimental details of the aforementioned attainments to increase mobility. And then interface polarization in the wurtzite crystals is discussed in terms of an empirical rule of wurtzite crystal chemistry. QHE in the ZnO/Mg<sub>x</sub>Zn<sub>1-x</sub>O interface is briefly described. The remainder of this article is a focus on the performance of the field-effect devices with the lattice-matched interface as high-mobility channels. The article ends with future prospects towards realizing oxide electronics.

## II. EPITAXIAL GROWTH

### A. Lattice-matched (0001) ScAlMgO<sub>4</sub>

We have been using ScAlMgO<sub>4</sub> (hereafter referred to SCAM) as a lattice-matched substrate material to grow ZnO heterostructures. SCAM has trigonal YbFe<sub>2</sub>O<sub>4</sub> structure ( $R\bar{3}m$ ), derived from cubic spinel, and its unit volume is the smallest among the isostructural crystals.<sup>23</sup> Followed after simple hexagonal expression for a trigonal system, its lattice constants are  $a = 0.3246$  nm and  $c = 2.5194$  nm. This crystal was first proposed by Hellman *et al.* for the use of substrate of GaN ( $a = 0.3189$  nm,  $c = 0.5185$  nm) and the high-quality single crystals were grown by the Czochralski method.<sup>24</sup>

Commercially available single crystal is highly transparent with no apparent color center [Fig. 2(a)]. Sc ions and (Mg, Al) ions alternately occupy octahedral sites and tetrahedral sites of the closed packed oxide ions, respectively. Its crystal structure can be regarded as a natural superlattice consisting of alternating stacks of wurtzite (0001)-face (Mg, Al)O<sub>x</sub> layer and rock-salt (111)-face ScO<sub>y</sub> layer along the  $c$ -axis. There is a strong cleavage habit along the (0001) plane. Figure 2(b) shows atomic configuration at the interface with ZnO, where both wurtzite blocks are coherently connected through the ScO<sub>y</sub> layer. An in-plane lattice mismatch with ZnO is rather smaller (0.09 % compressive) than that to GaN (1.8 % tensile). Accordingly, crystallinity of the ZnO could be substantially improved being comparable to that of high-quality bulk single crystal.<sup>25</sup> Mobility and residual carrier concentration of 1- $\mu$ m-thick films were 100 cm<sup>2</sup>/Vs and  $1 \times 10^{16}$  cm<sup>-3</sup>, respectively, at room temperature. As expected from the interface atomic arrangement shown in Fig. 2(b), the topmost film plane was found to be the O-face.

This substrate is suitable for characterization of optical and electronic properties because of wide band-gap of  $\sim 6.2$  eV, and hence, insulating nature. It is also

suitable to make a metal-insulator-semiconductor (MIS) and to demonstrate a  $p$ -type inversion layer at the interface between ZnO film and SCAM substrate.<sup>26</sup> We have fabricated a primary FET shown in inset of Fig. 3 and measured its characteristics by the following procedure.<sup>27</sup>

*Thin film growth:* Polished surface of (0001) SCAM substrates were cleaved along the (0001) plane to obtain atomically flat surface over several hundred micrometers wide area and to reduce the thickness down to approximately 100  $\mu\text{m}$ . Undoped ZnO films were grown on the substrates at 700°C by pulsed-laser deposition (PLD) equipped with reflection high-energy electron diffraction (RHEED).<sup>28</sup> ZnO single-crystal targets were ablated by KrF excimer laser pulses ( $\lambda = 248 \text{ nm}$ , repetition rate 5 Hz, laser fluence  $\sim 1 \text{ J/cm}^2$ ) with an oxygen flow of  $1 \times 10^{-6}$  Torr.

*Device fabrication and characterization:* The films were patterned by photolithography and ion milling to form Hall-bars. To ensure that the channel was fabricated in grain boundary-free region, the position of channels was selected on an area without bunched surface step, which was originated from imperfect cleavage process and was seen occasionally under optical microscope inspection. Metal electrodes consisted of Ti/Au were evaporated and patterned by lift-off. Pt wires were put on the electrodes by silver paste. Before polishing the backside of the substrate, the sample was glued on a glass substrate by a resin. Approximately 10  $\mu\text{m}$ -thick SCAM dielectric was reproducibly prepared by mechanical polishing and optical microscope inspection. Finally, the gate contacts were formed on the devices mounted on tip carrier (See inset of Fig. 3). Field-effect transfer characteristics and Hall-effect of the devices were measured at room temperature using a high-voltage gate source and a semiconductor parameter analyzer.

We once observed a behavior suggesting the presence of the  $p$ -type surface inversion layer, but the result was not verified due to poor reproducibility. A possible reason is that high-density defects exist at the ZnO/SCAM interface. Main panel of Fig. 3 shows the result of field-effect Hall measurement for a 20-nm-thick film. Hall mobility was actually very low, only  $\sim 10 \text{ cm}^2/\text{Vs}$ . Although it is unclear, the origin of such a severe carrier scattering could be positive charges at  $(\text{Sc}^{3+}\text{O}^{2-})^+$  layer in the vicinity of neutral  $(\text{Zn}^{2+}\text{O}^{2-})^0$  surface.

## **B. High-temperature annealed buffer layer**

Inserting buffer layer is often effective not only to reduce epitaxial strain but also to suppress deleterious influence of chemical dissimilarity between the film and substrate substances.<sup>29</sup> A strategy applied for large lattice-mismatch system is as follows. A highly disordered layer, usually the same material as that overgrown on it,

is first deposited on the substrate at low temperature. This layer is intended to be a sacrificing buffer layer for reducing epitaxial strain or for accommodating low-density nucleation sites and facilitating lateral growth during the subsequent high-temperature growth. In particular, the latter mechanism becomes dominant when crystallites existing occasionally in an amorphous matrix serve as preferential nucleation sites, which is exactly the situation established for the buffer layer of nitride semiconductors.

Instead of taking this standard technique, we chosen another kind of buffer layer that is what we call high-temperature annealed buffer layer (HITAB). The idea comes from interface dislocation engineering for (Ba,Sr)TiO<sub>3</sub> films on SrTiO<sub>3</sub> substrate.<sup>30</sup> High-temperature annealing for small lattice mismatch system is expected to yield two things, (1) misfit dislocations can be concentrated in a thin region near the film-substrate interface and accordingly residual strain can be removed, (2) migration of the surface atoms can be enhanced during the annealing to make surface atomically flat, a preferable configuration for minimizing surface energy and for realizing the layer-by-layer mode during overgrowth. If this situation is realized, overgrowth is essentially regarded as homoepitaxy on a self-template layer having perfect crystallinity.

*Thin film growth, high-temperature annealing and structural characterizations:* Using PLD, 1- $\mu\text{m}$ -thick undoped ZnO films were grown on lattice-mismatched (0001) sapphire and (0001) SCAM substrates in oxygen pressure ( $P_{\text{O}_2}$ ) of  $1 \times 10^{-6}$  Torr. The growth temperature on sapphire and SCAM substrates were 550°C and 650°C, respectively. The annealing was performed in air for 1 h at 1000°C, approximately corresponding to a half of the melting point of ZnO. For the films grown on SCAM substrates, *in-situ* annealing in a PLD chamber was also performed in  $P_{\text{O}_2} = 1$  mTorr. The surface morphology of the films was observed by atomic force microscopy (AFM) operated in contact mode. The crystal structure was examined by using a high-resolution x-ray diffraction (HRXRD) apparatus. Hall effect measurements were carried out at room temperature by using PPMS (Quantum Design). Hall bars with a channel area of  $60 \times 260 \mu\text{m}^2$  fabricated by using Ar ion etching and conventional photolithography technique. Ohmic electrodes consisting of Au/Ti layers were electron-beam-evaporated. Carrier density was evaluated from Hall resistivity measured with applying magnetic field up to  $\pm 1$  T.

Figure 4(a) shows AFM image of the as-grown film on the sapphire substrate. The annealing turned rough surface with characteristic grain structures into atomically flat surface as shown in Fig. 4(b). The height of surface steps corresponded to a half of the  $c$ -axis length (a charge neutral unit cell). It is found that the in-plane and out-of-plane lattice constants for the annealed film were the same as bulk values. However, the annealed film exhibited rather larger orientation tilting extracted from

reciprocal space XRD map, compared with the as-grown film.<sup>31</sup> Broad corrugations with approximately 1- $\mu$ m-spacing seen in the image suggest the presence of small-angle grain boundaries penetrating normal to the surface. Therefore, high-temperature annealing is not necessarily ideal technique to prepare buffer layer when lattice-mismatched substrate is used (Standard low-temperature buffer layer may be suitable in this case, but quality of the resulting film is not as good as that of the film grown on the HITAB layer on SCAM substrate.).

As for the film prepared on SCAM substrates, effect of the high-temperature annealing was totally different. Figure 4(c) shows AFM image of the as-grown film exhibiting roughness comparable to that for the annealed film grown in sapphire substrate. Similar corrugations seen in the image was not due to small-angle grain boundaries, but due to surface roughening because XRD rocking curve width was close to the resolution limit of the apparatus (18 arcseconds). The annealed film presented atomically flat terrace, as shown in Fig. 4(d), and lattice constants were the same as bulks. Clear RHEED intensity oscillation was observed during the entire growth of 1- $\mu$ m-thick films on the in-situ annealed buffer layers.<sup>20</sup> The results present ideal two-dimensional growth on the HITAB layer prepared on SCAM substrate,<sup>32</sup> opportunities not only for preparing high-quality undoped film but also for making *p*-type ZnO. In addition, application of this technique to  $Mg_xZn_{1-x}O$  resulted in improvement of alloy compositional homogeneity and reduction of concentration of point defects.<sup>33</sup>

Having established well-defined buffer layer, we investigated growth temperature dependence of surface morphology, which is shown in Figs. 5(a-e). Number of terrace level systematically decreased as growth temperature was increased from 800°C to 1000°C. It is noted that at 1000°C the entire surface is consisted of only two levels of atomically flat terrace, which is strikingly contrasted to the film grown directly on SCAM at 1000°C [Fig. 5(f)]. In this view, we analyzed the images shown in (a) to (e) and the results are summarized in Fig. 5(g). It is clearly seen that the minority levels representing “valley” gradually diminish and merge into higher majority levels with increasing growth temperature. This tendency suggests that migrating surface species gain kinetic energy enough to overcome energy barrier, *i.e.* Schwöbel barrier, and to move towards lower levels of terrace.<sup>34,35</sup> It is also worth noting that at lower temperatures (800 - 900°C) spacing of bench-like terraces surrounding peaks has considerably narrow distribution presenting a characteristic feature often seen when the effect of the Schwöbel barrier is pronounced.

The film grown on HITAB layer at 950°C exhibited the highest Hall mobility among the samples (300 cm<sup>2</sup>/Vs at room temperature), even higher than those obtained

for bulk crystals grown by vapor-phase transport technique.<sup>36-38</sup> Figure 6 shows residual carrier concentration and Hall mobility obtained in the quest for improving crystalline quality with using PLD and MBE.<sup>20,21,31,39-41</sup> The much higher mobility was achieved for our PLD films under the condition optimized by using temperature-gradient technique, details of which will be described in next paragraphs.

### C. Temperature-gradient epitaxy

It is well known that ZnO spontaneously exhibits *n*-type semiconducting properties because interstitial Zn ( $Zn_i$ ) or O vacancy ( $V_O$ ) is the most stable point defects.<sup>42</sup> In reality, impurities such as H, Al, and Ga, commonly found in commercial sources, also cause the electron doping. We examined the impurity level for a number of commercial sources by secondary ion mass spectroscopy analysis and concluded that single crystal grown by vapor-transport technique has the lowest impurity concentrations.<sup>43</sup> On the surface of supplied crystal, however, considerable amounts of NaCl and KCl were detected as verified in laser desorption-time of flight mass spectra as well as in SIMS depth profile. This fact makes us cautious especially when using a fresh target because those surface contaminants can cause an increase in the background carriers. A number of laser shots were required to reduce their intensity under the detection limit, while wet etching in a diluted aqueous nitric acid prior to the use sufficiently removed them. Remaining issue is only how to reduce intrinsic point defects that suppress the electron mobility.

Before going to details of the experiments for optimizing PLD growth condition of ZnO, let us consider about a widely accepted view for the MBE growth of binary compound semiconductors. In the case of III-V compounds, for example, there is an optimum flux ratio of III to V elements for obtaining high crystallinity with low defect concentration.<sup>44</sup> This is usually achieved at a temperature, where III-related surface species having sticking coefficient nearly unity gain enough kinetic energy to migrate over micrometers. At given optimum temperature and flux of V element, flux of III element is increased until growth rate is saturated, where right stoichiometry can be achieved. This is also the case for MBE growth of ZnO, where high mobility and narrow XRD rocking curve width are simultaneously achieved for the film grown under stoichiometric condition with a Zn flux optimized for given oxygen flux and growth temperature.<sup>45</sup> This fact implies that at a given flux ratio, there is an optimum growth temperature for obtaining the right stoichiometry.<sup>21</sup>

In case of the PLD growth, ablated vapor species are consisted of various kinds of particles including ions, exited neutral atoms and charged clusters.<sup>28</sup> In addition to these complex particles, the presence of oxygen molecules being dissociated to single

atoms before crystallization makes growth dynamics much more complicated compared with MBE.<sup>46</sup> We set the viewpoint for the MBE growth as a starting point and performed the experiments described below.

*Thin film growth and electrical characterizations:* ZnO/Mg<sub>0.15</sub>Zn<sub>0.85</sub>O bilayers were grown on SCAM substrates. Before growing top ZnO layers, the Mg<sub>0.15</sub>Zn<sub>0.85</sub>O layers were *in-situ* annealed to prepare semi-insulating and atomically-flat HITAB layers. 1- $\mu$ m-thick ZnO films were grown in  $P_{O_2} = 1 \times 10^{-7}$  Torr and  $1 \times 10^{-6}$  Torr. The growth temperature was varied by the temperature gradient technique, which allows us to grow the films in a wide range of growth temperature ( $\sim 200^\circ\text{C}$ ) on single substrate in a parallel fashion.<sup>47</sup> A PLD setup equipped with a semiconductor laser heating system is shown in Fig. 7(a). A substrate holder used for temperature-gradient epitaxy has a leg supported only at one ends, which was carefully designed for obtaining linear temperature gradient profile over 10-mm-long when another side of the leg is heated by focused infrared laser beam (cw, 808 nm) [Fig. 7(b)]. Persistent RHEED intensity oscillations were observed during ZnO thin film growth on the HITAB layers in the whole range of growth parameters. To minimize inhomogeneity in the electronic properties induced by temperature gradient within one measured region, resistivity and Hall measurements were performed for the array of small Hall-bars (Fig. 8). A range of temperature gradient within single device (60- $\mu$ m-wide) is less than  $2^\circ\text{C}$ .

The residual carrier density and Hall mobility at 300 K for all the samples are plotted against inverse of growth temperature in Figs 9(a) and 9(b), respectively. The solid lines are merely guide to the eyes. Apparently, carrier density for  $1 \times 10^{-6}$  Torr samples are systematically lower than those for  $1 \times 10^{-7}$  Torr samples regardless of growth temperature. The trends of carrier density for  $1 \times 10^{-7}$  Torr and  $1 \times 10^{-6}$  Torr films show kinks intersected by two broken straight lines having different slopes. Taking Arrhenius form of carrier density into account, two independent surface kinetics seem to dominate the formation of non-equilibrium defects that generate the free electrons. From the trend of Hall mobility, one can be noticed that the Hall mobility takes the singularly maximum values at certain growth temperatures marked by arrows, which coincides with the growth temperature giving the kinks for carrier density. Except for these anomalies, Hall mobility decreases as growth temperature increases, again exhibiting different slopes.

The result implies that the growth temperature giving mobility anomalies and kinks for carrier density at fixed  $P_{O_2}$  fulfill the stoichiometric conditions. We first note that intrinsic donors such as  $Zn_i$  and  $V_O$  must be major defects evolving at higher growth temperature and lower  $P_{O_2}$  according to conventional defect chemistry. This

situation seems to be realized at growth temperature higher than the anomalies because the steep increase of carrier density and the decrease of Hall mobility are seen with increasing growth temperature. The fact that anomaly for  $1 \times 10^{-6}$  Torr growth is higher than that for  $1 \times 10^{-7}$  Torr agrees with this viewpoint. Secondly, gradual slopes of carrier density and Hall mobility for growth temperatures below anomalies may come from the presence of acceptor-like defects in addition to the donors. Using time-resolved photoluminescence and monoenergetic positron annihilation spectroscopy, we have revealed that the concentration of Zn vacancy ( $V_{\text{Zn}}$ ) increases in our films as growth temperature is lowered from anomaly.<sup>48</sup> Similar experiment also verifies  $V_{\text{Zn}}$  assignable to an intrinsic acceptor.<sup>49</sup> Taken together, the appearance of anomalies can be understood in terms of the reduction of gross concentration of intrinsic donors and acceptors. A record-breaking mobility ( $440 \text{ cm}^2/\text{Vs}$ ) plotted in Fig. 6 was obtained for the films grown at  $975^\circ\text{C}$  in  $P_{\text{O}_2} = 1 \times 10^{-6}$  Torr.

### III. QUANTUM HALL EFFECT

#### A. Magnetotransport properties

We now describe the magnetotransport properties of the  $\text{ZnO}/\text{Mg}_x\text{Zn}_{1-x}\text{O}$  heterostructures prepared on SCAM substrate along the following procedure.

*Thin film growth and preparation of low-temperature transport samples:* Two different targets, namely, single-crystal high-purity ZnO (purchased from ZN Technology, Brea CA) and  $\text{Mg}_x\text{Zn}_{1-x}\text{O}$  ceramic ( $x = 0.06$  and  $0.1$ ) made in our laboratory, were used to grow ZnO and  $\text{Mg}_x\text{Zn}_{1-x}\text{O}$  layers ( $x = 0.15$  and  $0.20$ ), respectively. First, we prepared HITAB on SCAM substrates by growing a 100-nm-thick  $\text{Mg}_x\text{Zn}_{1-x}\text{O}$  layer at  $650^\circ\text{C}$  in  $P_{\text{O}_2} = 1 \times 10^{-6}$  Torr, followed by annealing at  $1000^\circ\text{C}$  in  $P_{\text{O}_2} = 1$  mTorr. The purpose of the HITAB is to prepare a strain-free and atomically flat template, which serves as a buffer layer for the overgrowth as we described before. This layer also acts as a potential barrier for the 2DEG in adjacent high-quality ZnO layer. The ZnO layers were subsequently grown in  $P_{\text{O}_2} = 1 \times 10^{-6}$  Torr by using temperature gradient technique.

The obtained films were processed in a conventional Hall-bar geometry by photolithography and Ar ion etching. Ohmic metal contacts consisting of Au/Ti layers were evaporated on the top film surface. The films outside the Hall devices were completely etched to electrically isolate each device. We also prepared samples with more direct contact geometry for buried  $\text{ZnO}/\text{Mg}_x\text{Zn}_{1-x}\text{O}$  heterointerfaces by removing top ZnO layers underneath the contact metals via etching. However, no difference was found in transport behavior between the devices having two types of contact geometries. The samples were mounted in a chip carrier, with electrical leads formed by wire

bonding, and were measured in a physical parameter measurement system (Quantum Design).

*Structural and electrical characterizations:* Structural characterization was performed using AFM and HRXRD (Panalytical, X'Pert MRD) in air at room temperature. HRXRD measurements revealed that the as-grown  $\text{Mg}_x\text{Zn}_{1-x}\text{O}$  layers had in-plane lattice constants identical to those of SCAM (3.246 Å), indicating a pseudomorphic epitaxial relationship. High-temperature annealing resulted in complete relaxation of the epitaxial strain. The surface of the annealed layers consisted of wide terraces and monolayer steps, as shown in the AFM image in Fig. 10(a). The resistivity of this film was more than  $10^2 \text{ } \Omega\text{cm}$  ( $10 \text{ M}\Omega/\square$ ) at room temperature, indicating that its contribution to current flow was negligible. The surface of the ZnO film grown on the HITAB layers was also atomically flat, as shown in Fig. 10(b).

Figure 10(c) shows the HRXRD pattern of a  $\text{ZnO}/\text{Mg}_{0.15}\text{Zn}_{0.85}\text{O}$  film (solid line) and a simulated pattern calculated using a one-dimensional step model (dotted line), in which an abrupt interface and an ideal homogeneous distribution of layer thickness were assumed. The good agreement between both patterns, including fine Laue structures, confirms that the heterointerface was abrupt and the ZnO layer was coherently grown on the relaxed  $\text{Mg}_{0.15}\text{Zn}_{0.85}\text{O}$  layer. Thus, the ZnO layer was under tensile biaxial strain in the plane.<sup>50</sup> We found that annealing of the  $\text{Mg}_x\text{Zn}_{1-x}\text{O}$  layers was important to create a high-mobility 2DEG at the heterointerfaces. In fact, when the  $\text{Mg}_x\text{Zn}_{1-x}\text{O}$  layer was unannealed, the mobility decreased as the measurement temperature decreased. For all of the samples discussed in the main paper, the full-width at half maximum of the rocking curve for the (0002) peak was less than 18 arcseconds (the instrument resolution).

We measured temperature dependence of sheet carrier density and Hall mobility for samples A, B and C (See Table II). At 1 K, the sheet carrier densities and Hall mobilities were  $0.66 \times 10^{12} \sim 3.7 \times 10^{12} \text{ cm}^{-2}$  and  $2700 \sim 5,500 \text{ cm}^2/\text{Vs}$ , respectively. It was found that sheet carrier density decreased as the temperature decreased. This suggests that some of the electrons distributed far away from the interfaces tend to be frozen out at low temperatures. Nevertheless, the mobility monotonically increased to reach a constant value below 1 K. We note that in the present films metallic conductivity was realized for such low sheet carrier densities samples. Considering reasonably high mobility, it is now feasible to observe QHE.

Figure 11 shows magnetic field dependence of longitudinal resistivity  $\rho_{xx}$  and Hall resistivity  $\rho_{xy}$  measured at low temperatures using a standard lock-in technique with AC excitation (10 nA, 19 Hz). At low field, all the samples exhibited negative

magnetoresistance, presumably due to weakly localized carriers. Above  $\sim 2$  T, clear SdH oscillations that were periodic in  $1/B$  appeared, their amplitudes increasing with increasing  $B$ . Although the zero-resistance state was absent due to the large scattering rate, each minimum of  $\rho_{xx}$  coincided with the quantized  $\rho_{xy}$  plateaus equal to  $h/e^2 \nu$ , where  $\nu$  is the Landau filling index. These observations confirmed the existence of the QHE in our samples and allowed direct determination of the 2DEG density ( $n_{2D}$ ), which systematically varied from ones obtained by low-field Hall resistivity.<sup>12</sup> We estimated the subband energies using a triangular-potential approximation<sup>51</sup>. The energy separations between the two lowest subband levels are greater than the Fermi energy, suggesting that in the temperature range of the experiments described here, carrier occupation in the second subband is negligible. In addition, effective well width was estimated to be  $4 \sim 6$  nm. From the temperature dependence of the SdH oscillation amplitude, the effective mass of the 2DEG was derived as  $0.32 \pm 0.03m_0$ .<sup>12</sup>

## B. Polarization induced charges

To analyze the experimentally measured carrier densities, we calculated the polarization induced charges. ZnO with a wurtzite structure is known to exhibit large spontaneous and piezoelectric polarization effects along the polar (0001) orientation.<sup>52,53</sup> These polarizations induce surface charges in the individual ZnO and  $Mg_xZn_{1-x}O$  layers, resulting in accumulation or depletion of free electrons at the heterointerfaces.<sup>54</sup> Since the growth orientation of our films was identified to be the O-face,<sup>55</sup> the direction of the spontaneous polarization was towards the surface [See Fig. 13(a)]. The spontaneous polarization  $P_{sp}$  of ZnO is reported to be  $-0.054$  C/m<sup>2</sup>.<sup>53</sup>

According to the HRXRD analysis described above, the piezoelectric polarization  $P_{pe}$  vanishes in unstrained  $Mg_xZn_{1-x}O$  layers, whereas in tensile-strained ZnO layers,  $P_{pe}$  should exist, having the same direction as  $P_{sp}$ . The magnitude of  $P_{pe}$  is proportional to the strain in the ZnO layer, which depends on  $x$  in the  $Mg_xZn_{1-x}O$  layers, and can be determined by,<sup>54</sup>

$$P_{pe} = 2\Delta a[e_{31}-e_{33}(C_{13}/C_{33})], \quad (1)$$

where  $\Delta a$  is the in-plane strain in the ZnO layer,  $e_{31}$  and  $e_{33}$  are piezoelectric coefficients, and  $C_{13}$  and  $C_{33}$  are elastic constants of ZnO. The value of  $\Delta a$  can be expressed as  $\Delta a = 0.027x^2 + 0.0083x$ .<sup>50</sup> The ratio of  $C_{13}/C_{33}$  is experimentally determined to be 0.5.<sup>56</sup> The experimental piezoelectric coefficients reported in Ref. 52 and references therein vary widely. We prefer to use those calculated from first principles, where the range of variation is relatively small for statistical accuracy. Taking these variations into

account,<sup>57-59</sup> Eq. (1) can be modified to

$$P_{\text{pc}}(x) = (1.98 \pm 0.28)(0.027x^2 + 0.0083x) \quad (\text{in C/m}^2). \quad (2)$$

Since there is no experimental data for  $P_{\text{sp}}$  in  $\text{Mg}_x\text{Zn}_{1-x}\text{O}$ , we use an empirical rule of wurtzite crystal chemistry to estimate it. In the ideal wurtzite compound MX (M and X are a cation and an anion, respectively), M is located at the center of the systematic X tetrahedron, so that the internal parameter  $u$  equals  $3/8$  ( $= 0.375$ ), and the four M-X bonds are equivalent. According to the simple point-charge model,  $P_{\text{sp}}$  vanishes in this case.<sup>53</sup> A geometric argument leads to an expression for  $u$  as a simple function of the lattice constants,

$$u = 1/3(a/c)^2 + 1/4. \quad (3)$$

In real wurtzite crystals, however,  $u$  is larger than  $0.375$  in a deformed X tetrahedron with three equivalent M-X bonds and one longer bond, giving rise to non-zero  $P_{\text{sp}}$ . In this case,  $P_{\text{sp}}$  can be expressed by

$$P_{\text{sp}} = [-8e/(\sqrt{3}a^2)](u-3/8), \quad (4)$$

again according to the point-charge model. Table III lists experimental lattice parameters of various wurtzite crystals reported in the literature.<sup>60-64</sup> Using these parameters, we plot the experimental  $u$  versus  $(a/c)^2$  in Fig. 12(a). A slight deviation between the linear fitting line (red) and dashed line representing the ideally deformed lattice given by Eq. (3) can be seen. Here, we assume that the fitting curve can be extrapolated for  $\text{Mg}_x\text{Zn}_{1-x}\text{O}$ , in which  $(a/c)^2$  systematically increases with increasing  $x$ . To confirm the validity of this assumption, we plot  $u$  versus  $(a/c)^2$  and  $P_{\text{sp}}$  versus  $u$  in Figs. 12(b) and 12(c), respectively, using theoretical values listed in Table IV.<sup>57-59,65-69</sup> The experimental and theoretical  $u$  versus  $(a/c)^2$  plots quantitatively agree with each other. In addition, the theoretical  $P_{\text{sp}}$  versus  $u$  plot approximately follows those calculated by Eq. (4) (closed triangles). Using experimental  $(a/c)^2$  values of  $\text{Mg}_x\text{Zn}_{1-x}\text{O}$ , we fitted the theoretical  $P_{\text{sp}}$  versus  $u$  to obtain  $\Delta P_{\text{sp}}(x) [= P_{\text{sp}}(x) - P_{\text{sp}}(0)]$  as follows:

$$\Delta P_{\text{sp}}(x) = -(0.17x^2 + 0.009x) \quad (\text{in C/m}^2), \quad (5)$$

which is plotted in Fig. 12(d) with a standard deviation of the least square fit.

This allows us to calculate the total sheet charge  $\sigma$  at the interface from Eqs. (2) and (5):

$$\sigma = [P_{\text{sp}}(0) + P_{\text{pe}}(x)] - P_{\text{sp}}(x) = |\Delta P_{\text{sp}}(x)| - |P_{\text{pe}}(x)| \quad (\text{in C/m}^2). \quad (6)$$

The density of sheet charge is simply calculated by dividing  $\sigma$  by the electron charge  $e$ . In Fig. 13(b), the calculated values of  $|\sigma/e|$ ,  $|\Delta P_{\text{sp}}(x)/e|$ , and  $|P_{\text{pe}}(x)/e|$  are plotted as a function of  $x$ . Here one finds that, when  $x$  is higher than  $\sim 0.1$ , polarization induced positive charges  $|\sigma/e|$  are formed at the heterointerfaces, and their density increases as  $x$  increases. There is good agreement between experimental carrier density (closed circles) and estimated  $|\sigma/e|$ , despite the ambiguity in  $P_{\text{pe}}(x)$ , a range of the theoretical values representing all of the shaded regions, and the lack of consideration of charge compensation with free electrons.<sup>54</sup> In Fig. 14, we compare our estimate for  $\Delta P_{\text{sp}}(x)$  with one obtained by *ab-initio* calculation that have been published after our study.<sup>70</sup> They show a good agreement, therefore we conclude that these values provide a useful parameter for designing band structures of various electric devices based ZnO/Mg<sub>x</sub>Zn<sub>1-x</sub>O interfaces.

The polarization effect and formation mechanism of the 2DEGs discussed above have been intensively studied for the isostructural GaN/Al<sub>x</sub>Ga<sub>1-x</sub>N interfaces.<sup>54</sup> Though only a few examples are known for the ZnO based heterointerfaces.<sup>70-72</sup>, there is a striking difference in both system that carrier density below  $1 \times 10^{13} \text{ cm}^{-2}$  is hardly achieved in the GaN/Al<sub>x</sub>Ga<sub>1-x</sub>N interface. This is because GaN layer grown on Al<sub>x</sub>Ga<sub>1-x</sub>N has tensile strain, in other words, the  $a$ -axis lattice constant of Al<sub>x</sub>Ga<sub>1-x</sub>N is systematically smaller than GaN, opposite to longer lattice constant of Mg<sub>x</sub>Zn<sub>1-x</sub>O than ZnO. As the result, the interface polarization charge equals to sum of spontaneous and piezoelectric polarizations in the GaN/Al<sub>x</sub>Ga<sub>1-x</sub>N interface, meaning that sign is plus in the third term of Eq. 6.<sup>54</sup> Thus, it is worth noting that sample A having the lowest carrier density exhibits Landau filling factor  $\nu = 2$ . This implies the exciting possibility of realizing the fractional QHE in the present heterostructure if the carrier mobility could be improved. In addition, given chemical compatibility with certain other classes of oxides, the quantized Hall state may be combined with a broad range of physical properties in a complex heterostructure.

## IV. FIELD-EFFECT TRANSISTORS

### A. Lattice-matched gate dielectrics

We have been searching for such gate dielectrics that can be epitaxially grown on the single crystalline ZnO channel for realizing high-mobility FET. Among a few

candidate materials having wider band-gap and small lattice mismatches to ZnO,  $\beta$ -LiGaO<sub>2</sub> (lattice mismatch = -2.6 %) <sup>73</sup> and SCAM (0.09 %) <sup>27</sup> were previously investigated. Although sharp interface and good crystalline quality were realized for both heterostructures, the electrical properties were not good enough to eliminate the defect density presumably due to chemical dissimilarity such as the valence mismatches at these heterointerfaces.

One can notice that a number of cubic rock-salt crystals have oxide ion distance comparable to that of ZnO and valences of cations same as that of Zn<sup>2+</sup>. The oxide ion distance in the hexagonal (111) plane is expressed  $a_{RS}/\sqrt{2}$ , where  $a_{RS}$  is the lattice constant of cubic lattice. If a solid solution consisted of such crystals can be epitaxially grown on (0001) plane of ZnO, the perfect lattice matching would be realized at an appropriate composition. Figure 15(a) shows band-gap plotted against oxide ion distance for various rock-salt oxides. Among several candidates, we have investigated Mg<sub>1-x</sub>Ca<sub>x</sub>O [Fig. 15(b)], which has sufficiently large band offset to ZnO. The  $a_{RS}$  of Mg<sub>1-x</sub>Ca<sub>x</sub>O is adjustable in a range between 4.211 Å (MgO) and 4.811 Å (CaO). A lattice mismatch arises from the difference in the spacing between neighboring oxygen ions and can be defined as  $(\sqrt{2}/2a_{RS}-a_{WZ})/a_{WZ}$ , where  $a_{WZ}$  is the  $a$ -axis lattice constant of wurtzite phase ZnO (3.250 Å). Thus, the lattice mismatch varies from -8.6 % to 4.4 % with increasing  $x$  from 0 to 1. We note that along the growth direction, stacking sequence of each cation atom and oxygen is identical to each other, and thus valence discontinuity does not exist in the heterointerfaces. It is also important to consider thermal expansion mismatch between Mg<sub>1-x</sub>Ca<sub>x</sub>O and ZnO. The thermal expansion coefficients are reported to be  $13.5 \times 10^{-6}$ ,  $12.8 \times 10^{-6}$ , and  $8.3 \times 10^{-6}$  /K for MgO, CaO, and ZnO at temperatures ranging from 20° C to 600° C, respectively. <sup>74</sup> The thermal expansion mismatches estimated from these values are 0.20 % and 0.17 % for MgO/ZnO and CaO/ZnO, respectively, as temperature decreases from 400° C to room temperature.

The epitaxial growth of the solid solutions has been previously demonstrated by Hellman *et al.* using MBE. <sup>75</sup> The miscibility gap was found to be absent in the films grown on (100) MgO substrates. This was despite small solubility (less than 2 mol% in both end members) of MgO-CaO system known in a bulk form. <sup>76</sup> They observed linear compositional dependence of the lattice constants. These facts lead us to examine the heteroepitaxial growth of this metastable oxide on ZnO. However, the composition of Mg<sub>1-x</sub>Ca<sub>x</sub>O has to be controlled accurately because a slight deviation from the optimal composition readily induces a large lattice mismatch. Therefore, we applied composition spread technique to grow Mg<sub>1-x</sub>Ca<sub>x</sub>O films including the perfectly lattice-matched films to ZnO. <sup>77</sup>

*Thin film growth and structural characterization:* Target materials were prepared from reagent grade MgO and CaCO<sub>3</sub> powders. Before weighing, the MgO powder was heated at 1000° C. The weighed batches were fired at 1000° C for 12 h in air. To improve homogeneity, the mixtures were ground and again reacted at 1300 ° C for 12 h. Dense pellets having various CaO compositions were obtained. Single-composition films and composition-spread films (approximately 200 nm-thick) were grown on ZnO layers (300 nm-thick) on (0001) SCAM substrates by PLD. Growth temperature was 700° C, while  $P_{O_2}$  was fixed at  $1 \times 10^{-6}$  Torr. The as-grown films were characterized by HRXRD.

The films exhibited the (111) oriented rock-salt phase without any precipitates of the end members. Figure 16 shows x-ray diffraction reciprocal lattice maps for the films having the Ca content of 0.43, 0.53 and 0.58, indicating relaxed lattices with lattice constants nearly same as bulk. It is seen that nearly perfect lattice matching is achieved at  $x = 0.58$ . In addition, any evidence of interdiffusion at the heterointerfaces was not detected as verified by sharp excitonic peaks in the absorption spectra of underlying ZnO for all the films. Remarkable stability of metastable Mg<sub>1-x</sub>Ca<sub>x</sub>O solid solutions was previously accounted in terms of epitaxial quenching.<sup>75</sup>

Having established a coherent interface between lattice-matched Mg<sub>0.42</sub>Ca<sub>0.58</sub>O gate dielectric and ZnO, we fabricated FET (channel area  $5 \times 15 \mu\text{m}^2$ ) by depositing another gate dielectric layer (a-Al<sub>2</sub>O<sub>3</sub>) on the top of the Mg<sub>0.42</sub>Ca<sub>0.58</sub>O layer [See Fig. 1(c)]. Figure 17(a) shows typical output characteristics at room temperature, exhibiting clear saturation behavior. Field-effect mobility extracted from transfer characteristics shown in Fig. 17(b) was as high as  $250 \text{ cm}^2/\text{VS}$ . In addition, threshold voltage  $V_{\text{th}}$  and subthreshold swing was as small as -0.1 V and 0.2 V/decade, respectively. The results indicate an excellent FET performance being promising for practical application.

## **B. Low temperature properties**

There are very few attempts of investigating low-temperature magnetotransport in wide band-gap oxide semiconductors based FETs. In practice, it is an essential approach for improvement of device performance as well as understanding device physics.<sup>78,79</sup> Our recent observation of the QHE in Mg<sub>x</sub>Zn<sub>1-x</sub>O/ZnO heterostructures opens a promising opportunity for such a study. One of the particular interests is field-effect control of Landau filling factor in 2DEG. As we described already (Sec. III-B), the 2DEG density can be controlled with varying Mg content and donor concentration in the well layer. The growth polarity (O- or Zn-polar) is a primary factor because it determines the directions of the spontaneous and piezoelectric

polarizations and resulting potential energy gradient. Two configurations are possible to induce 2DEG at the interfaces: the O-polar ZnO on  $\text{Mg}_x\text{Zn}_{1-x}\text{O}$  and the Zn-polar  $\text{Mg}_x\text{Zn}_{1-x}\text{O}$  on ZnO. There are several reports for both cases, where the former is grown by PLD,<sup>12</sup> whereas the latter is grown by MBE.<sup>72,80,81</sup>

We employed atomic-layer-deposited amorphous  $\text{Al}_2\text{O}_3$  gate dielectric to accumulate 2DEG in an O-polar double heterostructure, where polarization mismatch was designed to be very small.<sup>12</sup> Atomic layer deposition (ALD) attracts increasing interest owing to its superiority for preparation of reliable gate dielectrics on a wide spectrum of materials.<sup>82-86</sup> High breakdown field and low trap density make it possible to perform stable measurements under high electric field.

*Thin film growth and device fabrication:* The ZnO/ $\text{Mg}_x\text{Zn}_{1-x}\text{O}$  double heterostructure was prepared on insulating (0001) SCAM substrate. The sample consists of a top layer of 50-nm-thick  $\text{Mg}_{0.12}\text{Zn}_{0.88}\text{O}$ , and an 100-nm-thick ZnO layer, and a bottom layer of 100-nm-thick  $\text{Mg}_{0.12}\text{Zn}_{0.88}\text{O}$ . The bottom  $\text{Mg}_{0.12}\text{Zn}_{0.88}\text{O}$  layer was grown at 650 °C and annealed at 1000 °C in 1 mTorr of oxygen for making its surface atomically flat. The growth temperature for the ZnO layer and the top  $\text{Mg}_{0.12}\text{Zn}_{0.88}\text{O}$  layer was set at 950 °C. Standard Hall bars with a channel area of  $60 \times 260 \mu\text{m}^2$  were fabricated by using Ar ion etching and conventional photolithography technique. Using an ALD apparatus, a 40-nm-thick amorphous  $\text{Al}_2\text{O}_3$  gate dielectric was deposited at 150 °C.<sup>85</sup> Ohmic and gate electrodes consisting of Au/Ti layers were electron-beam-evaporated.

Figure 18 illustrates difference in sample structures, conduction band diagrams, and locations of 2DEG between previously discussed metallic heterostructures (top) and the present field-effect device (bottom). Both samples have the same configurations (O-polar, compressively strained ZnO layers, and unstrained  $\text{Mg}_x\text{Zn}_{1-x}\text{O}$  layers), and the directions of  $P_{\text{sp}}$  and  $P_{\text{pe}}$  are rightward towards the surface. When  $x$  is higher than  $\sim 0.1$ , sum of  $|P_{\text{sp}}|$  and  $|P_{\text{pe}}|$  in ZnO layer is considerably larger than  $|P_{\text{sp}}|$  in  $\text{Mg}_x\text{Zn}_{1-x}\text{O}$ . Therefore, positive charges formed at the ZnO/ $\text{Mg}_x\text{Zn}_{1-x}\text{O}$  interface induce 2DEG in the side of ZnO. As shown in Fig. 18(a), this is the case for the metallic heterostructures with  $x \geq 0.15$ , given sufficiently high donor concentrations in ZnO grown at high temperature. Instead, we chose a set of parameters of both relatively lower  $x$  and lower growth temperature, which is expected to result in nearly flat band and low donor concentration in ZnO layer. In fact, the left channel was “off” for the present film, exhibiting a semi-insulating conduction without gating, and a metallic “on” state appeared under applied positive gate bias, as will be described below. This clearly indicates that 2DEG was accumulated at the right of ZnO layer with electric field gating through atomic-layer-deposited  $\text{Al}_2\text{O}_3$ , a high mobility channel being formed at clean

epitaxial interface with right  $\text{Mg}_x\text{Zn}_{1-x}\text{O}$  layer [See Fig. 18(b)].

Our device showed a typical  $n$ -type FET behavior in its output characteristics. Low-temperature magnetotransport measurements were carried out with lock-in technique in a physical properties measurement system (PPMS, Quantum Design). A series standard resistance of 1 M $\Omega$  was inserted into measurement circuit for current correction. Figure 19(a) shows drain current  $I_D$  versus drain voltage  $V_D$  measured at 2 K after each incremental change of gate voltage  $V_G$  by 1 V. Systematic  $V_G$  dependence of longitudinal resistance  $\rho_{xx}$  shown in inset indicates that carriers were accumulated at the right interface. Through all of the measurements, gate leakage current was suppressed below 10 pA.

Hall effect was measured at 2 K with applying magnetic field up to  $\pm 1$  T,  $V_G$  ranging from 2 V to 8 V, and an ac excitation of 1  $\mu\text{A}$ . Note that Hall effect in the linear region was sufficiently characterized under the given ranges of  $V_G$  and  $I_D$ . Both of carrier density  $n$  and mobility  $\mu$  increased with increasing  $V_G$ , but the increase in the latter was more dramatic due to rapid evolution of screening effect [Fig. 18(b)]. The  $n$  could be increased up to  $1.2 \times 10^{12} \text{ cm}^{-2}$  by applying  $V_G = 8$  V. From linear  $V_G$  dependence of  $n$ , we extracted an effective capacitance of stacking layers (40-nm-thick  $\text{Al}_2\text{O}_3$  and 50-nm-thick  $\text{Mg}_{0.12}\text{Zn}_{0.88}\text{O}$ ) to be  $\sim 20 \text{ nF/cm}^2$ . Indeed, the highest value of  $\mu$  was recorded to be  $5000 \text{ cm}^2/\text{Vs}$  at  $V_G = 7$  V, which is comparable to those for a metallic  $\text{ZnO}/\text{Mg}_{0.2}\text{Zn}_{0.8}\text{O}$  heterostructures (See Table II). Thus, it is concluded that location of 2DEG does not affect the magnitude of  $\mu$  in our devices.

We note that all of our PLD-grown films exhibit lower  $\mu$  than that obtained for Zn-polar films grown by MBE ( $14000 \text{ cm}^2\text{V}^{-1}\text{s}^{-1}$ ).<sup>80</sup> It is most likely due to the difference in concentrations of unintentionally doped impurities such as Si and Al in  $\text{Mg}_x\text{Zn}_{1-x}\text{O}$  barrier layers. In fact, the  $\text{Mg}_x\text{Zn}_{1-x}\text{O}$  ceramic targets as starting materials for PLD growth have inevitable large amounts of the impurities, which also reflects its optical properties inferior to that of the MBE-grown  $\text{Mg}_x\text{Zn}_{1-x}\text{O}$ .<sup>32,33,88,89</sup> Therefore, the MBE-grown sample is much suitable to further study of field-effect control of 2DEG, which will be published elsewhere.<sup>90</sup>

Figure 20 shows temperature dependence of  $\rho_{xx}$  measured at zero-magnetic field by applying  $V_G$  ranging from -2 V to 6 V. Insulating behavior ( $d\rho_{xx}/dT < 0$ ) was seen when  $V_G \leq 2$  V, while metallic “on” state ( $d\rho_{xx}/dT > 0$ ) appeared when  $V_G \geq 4$  V. We note that an insulator-to-metal transition (IMT) took place below quantum resistance  $h/e^2$ , being consistent with the behavior expected for a two-dimensional system around 2 K.<sup>87</sup> From Fig. 19(b), a critical carrier density ( $n_c$ ) is identified to be  $\sim 6 \times 10^{11} \text{ cm}^{-2}$ , which is comparable to that observed for a photoinduced IMT in a  $\text{ZnO}/\text{Mg}_{0.15}\text{Zn}_{0.85}\text{O}$  heterostructure.<sup>91</sup> Compared to conventional 2DEG systems, the observed  $n_c$  is one

order of magnitude higher, but it can actually be decreased when the  $\mu$  is improved by the use of MBE.<sup>90</sup> Peak mobility and  $n_c$  at IMT in ZnO/Mg<sub>x</sub>Zn<sub>1-x</sub>O interfaces are summarized in Table V.

Unlike room-temperature characteristics in previously reported wide band-gap semiconductors based FETs, low-temperature mobility of our device showed remarkably large enhancement, more than one order of magnitude as carrier density was doubled from  $6 \times 10^{11} \text{ cm}^{-2}$ . As a result,  $\mu$  reached  $5000 \text{ cm}^2\text{V}^{-1}\text{s}^{-1}$  across clear IMT, which confirms current upper bound for  $\mu$  attainable in PLD grown FETs. Ionized or neutral impurities in Mg<sub>x</sub>Zn<sub>1-x</sub>O layers are thought to be predominant carrier scattering centers. Although the observed SdH oscillations and Hall plateaus was not very clear, partly due to high temperature measurement,<sup>92</sup> our experiments clearly demonstrate the possibility of electric-field control of quantum phase transition in diluted 2DEG at oxide semiconductor heterointerface.

## V. Conclusions

An atomic-scale control of surface and interface in ZnO heterostructures are reported. We have continued to improve epitaxial growth technology of ZnO since 1997, when we succeeded in observing ultraviolet laser emission at room temperature. The performance of the developed devices such as light-emitting diodes and field-effect transistors is now confirmed through the observation of the QHE, which emerges only in exceptionally high-quality semiconductors.

The experiments conducted by us aim at achieving transparent electronics. The extreme target of transparent electronics is to make elements transparent while maintaining the current properties of integrated circuits. The existence of transparent objects is not as apparent to people, so the objects can be applied in various ways in the ubiquitous network society. Such applications include security sensors, invisible electronic tags, and transparent displays. An electronic display system that appears transparent as a windowpane could come into practical use in the not-too-distant future.

Perhaps the other significance of the experiments we have conducted lies in ushering in the field of oxide electronics,<sup>93</sup> which includes transparent electronics, through the development of oxide semiconductors of practical grade. It is not an exaggeration to say that the innovations in electronics technology that support today's economic growth have been brought about by the semiconductor research that has undergone rapid progress since the 1950s and the consequent improvements in crystal growth technology. The technological developments in crystal growth were only possible through consistent efforts and through trial and error, and the process has been repeated with the realization that high-quality crystals led to the innovation of new

electronic devices. Developments in integration technology of silicon semiconductors will inevitably come to an end in the near future. Instead, a great deal is expected of alternative technology that enables the application of diverse physical properties of oxides as device functions.

The semiconductor materials developed to date consist of typical elements from the III, IV, and V families, and many of them contain toxic elements that could pollute the environment. On the other hand, many of wide band-gap oxide semiconductors are chemically stable and biologically harmless, and are attractive materials that occur in abundant quantities in nature. We hope our study would facilitate further progress in the area, and there is no doubt that the history of improvement in crystal growth technology and the consequent development of high-quality devices will be repeated also with ionic crystals other than oxides and organic semiconductors.

### **Acknowledgements**

The authors thank Dr. T. Kita and Dr. D. Chiba for their expert assistances regarding low-temperature magnetotransport measurements and atomic layer deposition and Prof. H. Ohno and Prof. Y. Ohno for stimulated discussion regarding QHE. This work was partially supported by the Asahi Glass Foundation.

## References

1. T. Ando, A. B. Fowler, and F. Stern, *Rev. Mod. Phys.* **54**, 437 (1982).
2. D. Eger and Y. Goldstein, *Phys. Rev. B* **19**, 1089 (1979).
3. M. Nitzan, Y. Grinshpan, and Y. Goldstein, *Phys. Rev. B* **19**, 4107 (1979).
4. E. Veuhoff and D. Kohl, *J. Phys. C* **14**, 2395 (1981).
5. K. v. Klitzing, G. Dorda, and M. Pepper, *Phys. Rev. Lett.* **45**, 494 (1980).
6. J. Wakabayashi and S. Kawaji, *J. Phys. Soc. Jpn.* **44**, 1839 (1978).
7. R. People, J. C. Bean, D. V. Lang, A. M. Sergent, H. L. Stormer, K. W. Wecht, R. T. Lynch, and K. Boldwin, *Appl. Phys. Lett.* **45**, 1231 (1984).
8. N. P. Ong, J. K. Moyle, J. Bajaj, and J. T. Cheung, *J. Vac. Sci. Technol. A* **5**, 3079 (1987).
9. D. C. Tsui and A. C. Gossard, *Appl. Phys. Lett.* **38**, 550 (1981).
10. Y. Guldner, J. P. Vieren, P. Voisin, M. Voos, M. Razeghi, and M. A. Poisson, *Appl. Phys. Lett.* **40**, 877 (1982).
11. R. Gaska, J. W. Yang, A. Osinsky, Q. Chen, M. A. Khan, A. O. Orlov, G. L. Snider, and M. S. Shur, *Appl. Phys. Lett.* **72**, 707 (1998).
12. A. Tsukazaki, A. Ohtomo, T. Kita, Y. Ohno, H. Ohno, and M. Kawasaki, *Science* **315**, 1388 (2007).
13. A. Ohtomo and H. Y. Hwang, *Nature* **427**, 423 (2004).
14. K. Ellmer and R. Mientus, *Thin Solid Films* **516**, 4620 (2008).
15. J. Nishii, F. M. Hossain, S. Takagi, T. Aita, K. Saikusa, Y. Ohmaki, I. Ohkubo, S. Kishimoto, A. Ohtomo, T. Fukumura, F. Matsukura, Y. Ohno, H. Koinuma, H. Ohno, and M. Kawasaki, *Jpn. J. Appl. Phys.* **42**, L347 (2003).
16. F. M. Hossain, J. Nishii, S. Takagi, A. Ohtomo, T. Fukumura, H. Fujioka, H. Ohno, H. Koinuma, and M. Kawasaki, *J. Appl. Phys.* **94**, 7768 (2003).
17. J. Nishii, A. Ohtomo, K. Ohtani, H. Ohno, and M. Kawasaki, *Jpn. J. Appl. Phys.* **44**, L1193 (2005).
18. J. Nishii, A. Ohtomo, M. Ikeda, Y. Yamada, K. Ohtani, H. Ohno, and M. Kawasaki, *Appl. Surf. Sci.* **252**, 2507 (2006).
19. J. Nishii, A. Ohtomo, K. Ohtani, H. Ohno, and M. Kawasaki, unpublished.
20. A. Tsukazaki, A. Ohtomo, T. Onuma, M. Ohtani, T. Makino, M. Sumiya, K. Ohtani, S. F. Chichibu, S. Fuke, Y. Segawa, H. Ohno, H. Koinuma, and M. Kawasaki, *Nat. Mater.* **4**, 42 (2005).
21. A. Tsukazaki, A. Ohtomo, and M. Kawasaki, *Appl. Phys. Lett.* **88**, 152106 (2006).
22. A. Ohtomo, *The Japan Journal* **4**, 27 (2007).
23. N. Kimizuka and T. Mohri, *J. Solid State Chem.* **78**, 98 (1989).
24. E. S. Hellman, C. D. Brandle, L. F. Schneemeyer, D. Wiesmann, I. Brener, T.

- Siegrist, G. W. Berkstresser, D. N. E. Buchanan, and E. H. Hartford, *Internet J. Nitrides Semicond. Res.* **1**, 1 (1996).
25. A. Ohtomo, K. Tamura, K. Saikusa, K. Takahashi, T. Makino, Y. Segawa, H. Koinumab, and M. Kawasaki, *Appl. Phys. Lett.* **75**, 2635 (1999).
  26. H. Saito, A. Tsukazaki, K. Tamura, C. Hirose, H. Koinuma, and M. Kawasaki, *Ext. Abstr. Part I*, p. 216 (62th Spring Meet. 2001); Japan Society of Applied Physics, and Related Societies.
  27. T. I. Suzuki, A. Ohtomo, A. Tsukazaki, F. Satoh, J. Nishii, H. Ohno, and M. Kawasaki, *Adv. Mater.* **16**, 1887 (2004).
  28. A. Ohtomo and A. Tsukazaki, *Semicond. Sci. Technol.* **20**, S1 (2005).
  29. M. Kawasaki, K. Terai, A. Tsukazaki, T. Ohnishi, A. Ohtomo, and M. Lippmaa, *Nihon Kessho Seicho Gakkaishi*, **32**, 74 (2005) (in Japanese).
  30. K. Terai, M. Lippmaa, P. Ahmet, T. Chikyow, T. Fujii, H. Koinuma, and M. Kawasaki, *Appl. Phys. Lett.* **80**, 4437 (2002).
  31. A. Ohtomo, H. Kimura, K. Saito, T. Makino, Y. Segawa, H. Koinuma, and M. Kawasaki, *J. Cryst. Growth* **214/215**, 284 (2000).
  32. A. Tsukazaki, A. Ohtomo, S. Yoshida, M. Kawasaki, C. H. Chia, T. Makino, Y. Segawa, T. Koida, S. F. Chichibu, and H. Koinuma, *Appl. Phys. Lett.* **83**, 2784 (2003).
  33. M. Kubota, T. Onuma, A. Tsukazaki, A. Ohtomo, M. Kawasaki, T. Sota, and S. F. Chichibu, *Appl. Phys. Lett.* **90**, 141903 (2007).
  34. R. L. Schwöbel and E. J. Shipsey, *J. Appl. Phys.* **37**, 3682 (1966).
  35. R. L. Schwöbel, *J. Appl. Phys.* **40**, 614 (1969).
  36. D. C. Look, D. C. Reynolds, J. R. Sizelove, R. L. Jones, C. W. Litton, G. Cantwell, and W. C. Harsch, *Solid State Commun.* **105**, 399 (1998).
  37. D. C. Look, J. W. Hemsky, and J. R. Sizelove, *Phys. Rev. Lett.* **82**, 2552 (1999).
  38. D. C. Look, G. C. Farlow, P. Reunchan, S. Limpijumnong, S. B. Zhang, and K. Nordlund, *Phys. Rev. Lett.* **95**, 225502 (2005).
  39. S. Choopun, R. D. Vispute, W. Noch, A. Balsamo, R. P. Sharma, T. Venkatesan, A. Iliadis, and D. C. Look, *Appl. Phys. Lett.* **75**, 3947 (1999).
  40. A. Tsukazaki, H. Saito, K. Tamura, M. Ohtani, H. Koinuma, M. Sumiya, S. Fuke, T. Fukumura, and M. Kawasaki, *Appl. Phys. Lett.* **81**, 235 (2002).
  41. H. Tampo, A. Yamada, P. Fons, H. Shibata, K. Matsubara, K. Iwata, S. Niki, K. Nakahara, and H. Takasu, *Appl. Phys. Lett.* **84**, 4412 (2004).
  42. G. Neumann, *Current Topics in Materials Science* (1981). Vol 7, Sec. 3.
  43. M. Sumiya, S. Fuke, A. Tsukazaki, K. Tamura, A. Ohtomo, M. Kawasaki, and H. Koinuma, *J. Appl. Phys.* **93**, 2562 (2003).
  44. R. F. C. Farrow, *Molecular Beam Epitaxy* (Noyes, Park Ridge, NJ, 1995).

45. H. Kato, M. Sano, K. Miyamoto, and T. Yao, *Jpn. J. Appl. Phys. Part 1*, **42** 2241 (2003).
46. A. Ohtomo and H. Y. Hwang, *J. Appl. Phys.* **102**, 083704 (2007).
47. A. Tsukazaki, H. Saito, K. Tamura, M. Ohtani, H. Koinuma, M. Sumiya, S. Fuke, T. Fukumura, and M. Kawasaki, *Appl. Phys. Lett.* **81**, 235 (2002).
48. A. Uedono, T. Koida, A. Tsukazaki, M. Kawasaki, Z. Q. Chen, S. F. Chichibu, and H. Koinuma, *J. Appl. Phys.* **93**, 2481 (2003).
49. S. F. Chichibu, A. Uedono, A. Tsukazaki, T. Onuma, M. Zamfirescu, A. Ohtomo, A. Kavokin, G. Cantwell, C. W. Litton, T. Sota, and M. Kawasaki, *Semicond. Sci. Technol.* **20**, S67 (2005).
50. A. Ohtomo, M. Kawasaki, T. Koida, K. Masubuchi, H. Koinuma, Y. Sakurai, Y. Yoshida, T. Yasuda, and Y. Segawa, *Appl. Phys. Lett.* **72**, 2466 (1998).
51. F. Stern, *Phys. Rev. B* **5**, 4891 (1972).
52. I. B. Kobiakov, *Solid State Commun.* **35**, 305 (1980).
53. J. Jerphagnon and H. W. Newkirk, *Appl. Phys. Lett.* **18**, 245 (1971).
54. O. Ambacher, B. Foutz, J. Smart, J. R. Shealy, N. G. Weimann, K. Chu, M. Murphy, A. J. Sierakowski, W. J. Schaff, L. F. Eastman, R. Dimitrov, A. Mitchell, and M. Stutzmann, *J. Appl. Phys.* **87**, 334 (2000).
55. T. Ohnishi, A. Ohtomo, M. Kawasaki, K. Takahashi, M. Yoshimoto, and H. Koinuma, *Appl. Phys. Lett.* **72**, 824 (1998).
56. T. Makino, T. Yasuda, Y. Segawa, A. Ohtomo, K. Tamura, M. Kawasaki, and H. Koinuma, *Appl. Phys. Lett.* **79**, 1282 (2001).
57. A. D. Corso, M. Posternak, R. Resta, and A. Baldereschi, *Phys. Rev. B* **50**, 10715 (1994).
58. F. Bernardini, V. Fiorentini, and D. V. anderbilt, *Phys. Rev. B* **56**, R10024 (1997).
59. Y. Noel *et al.*, *Phys. Rev. B* **65**, 014111 (2001).
60. T. Ogawa, *J. Phys. Soc. Jpn.* **25**, 1126 (1968).
61. S. C. Abrahams and J. L. Bernstein, *Acta Cryst. B* **25**, 1233 (1969).
62. T. M. Sabine and S. Hogg, *Acta Cryst. B* **25**, 2254 (1969).
63. H. Schulz and K. H. Thiemann, *Solid State Commun.* **23**, 815 (1977).
64. H. Schulz and K. H. Thiemann, *Solid State Commun.* **32**, 783 (1979).
65. C. Y. Yeh, Z. W. Lu, S. Froyen, and A. Zunger, *Phys. Rev. B* **46**, 10086 (1992).
66. A. F. Wright and J. S. Nelson, *Phys. Rev. B* **50**, 2159 (1994).
67. K. Kim, W. R. L. Lambrecht, and B. Segall, *Phys. Rev. B* **53**, 16310 (1996).
68. K. Kim, W. R. L. Lambrecht, and B. Segall, *Phys. Rev. B* **56**, 7018 (1997).
69. P. Gopal and N. A. Spaldin, *J. Electro. Mater.* **35**, 538 (2006).
70. A. Malashevich and D. V. anderbilt, *Phys. Rev. B* **75**, 045106 (2007)

71. K. Koike, K. Hama, I. Nakashima, S. Sasa, M. Inoue, and M. Yano, *Jpn. J. Appl. Phys.* **44**, 3822 (2005).
72. H. Tampo, H. Shibata, K. Matsubara, A. Yamada, P. Fons, S. Niki, M. Yamagata, and H. Kanie, *Appl. Phys. Lett.* **89**, 132113 (2006).
73. I. Ohkubo, C. Hirose, K. Tamura, J. Nishii, H. Saito, H. Koinuma, P. Ahemt, T. Chikyow, T. Ishii, S. Miyazawa, Y. Segawa, T. Fukumura, and M. Kawasaki, *J. Appl. Phys.* **92**, 5587 (2002).
74. J. Talvacchio, J. R. Gavaler, and A. I. Braginski, *Metallic Multilayers and Epitaxy*, edited by M. Hong, S. Wolf, D. C. Gubser, (The Metallurgical Society, Warrendale, 1988), p. 109.
75. E. S. Hellman and E. H. Hartford, Jr., *Appl. Phys. Lett.* **64**, 1341 (1994).
76. R. C. Doman, J. B. Barr, R. N. McNally, A. M. Alper, *J. Am. Ceram. Soc.* **46**, 313 (1963)
77. J. Nishii, A. Ohtomo, M. Ikeda, Y. Yamada, K. Ohtani, H. Ohno, and M. Kawasaki, *Appl. Surf. Sci.* **252**, 2507 (2006).
78. K. Shibuya, T. Ohnishi, T. Uozumi, T. Sato, M. Lippmaa, M. Kawasaki, K. Nakajima, T. Chikyow, and H. Koinuma, *Appl. Phys. Lett.* **88**, 212116 (2006).
79. H. Nakamura, H. Takagi, I. H. Inoue, Y. Takahashi, T. Hasegawa, and Y. Tokura, *Appl. Phys. Lett.* **89**, 133504 (2006).
80. A. Tsukazaki, H. Yuji, S. Akasaka, K. Tamura, K. Nakahara, T. Tanabe, H. Takasu, A. Ohtomo, and M. Kawasaki, *Appl. Phys. Express* **1**, 055004 (2008).
81. K. Koike, K. Hama, I. Nakashima, G. Takada, M. Ozaki, K. Ogata, S. Sasa, M. Inoue, and M. Yano, *Jpn. J. Appl. Phys.* **43**, L1372 (2004).
82. P. D. Ye, G. D. Wilk, J. Kwo, B. Yang, H. J. Gossmann, M. Frei, S. N.G. Chu, J. P. Mannaerts, M. Sergent, M. Hong, K. K. Ng, and J. Bude, *IEEE Electron Device Lett.* **24**, 209 (2003).
83. K. Lai, P. D. Ye, W. Pan, D. C. Tsui, S. A. Lyon, M. Muhlberger, and F. Schaffler, *Appl. Phys. Lett.* **87**, 142103 (2005).
84. T. M. Lu, J. Liu, J. Kim, K. Lai, D. C. Tsui, and Y. H. Xie, *Appl. Phys. Lett.* **90**, 182114 (2007).
85. D. Chiba, F. Matsukura, and H. Ohno, *Appl. Phys. Lett.* **89**, 162505 (2006).
86. P. F. Carcia, R. S. McLean, and M. H. Reilly, *Appl. Phys. Lett.* **88**, 123509 (2006).
87. E. Abrahams, S. V. Kravchenko, and M. P. Sarachik, *Rev. Mod. Phys.* **73**, 251 (2001).
88. H. Yuji, K. Nakahara, K. Tamura, S. Akasaka, A. Sasaki, T. Tanabe, H. Takasu, T. Onuma, S. F. Chichibu, A. Tsukazaki, A. Ohtomo, and M. Kawasaki, *Proc. of SPIE*, **6895**, 68950D (2008).

89. Y. Nishimoto, K. Nakahara, D. Takamizu, A. Sasaki, K. Tamura, S. Akasaka, H. Yuji, T. Fujii, T. Tanabe, H. Takasu, A. Tsukazaki, A. Ohtomo, T. Onuma, S. F. Chichibu, and M. Kawasaki, *Appl. Phys. Express* **1**, 091202 (2008).
90. M. Nakano, A. Tsukazaki, K. Ueno, S. Akasaka, H. Yuji, K. Tamura, K. Nakahara, T. Tanabe, A. Kamisawa, T. Fukumura, A. Ohtomo, and M. Kawasaki, unpublished.
91. A. Tsukazaki, A. Ohtomo, M. Nakano, and M. Kawasaki, *Appl. Phys. Lett.* **92**, 052105 (2008).
92. A. Tsukazaki, A. Ohtomo, D. Chiba, Y. Ohno, H. Ohno, and M. Kawasaki, *Appl. Phys. Lett.* **93**, 241905 (2008).
93. A. P. Ramirez, *Science* **315**, 5817 (2007).

**Table I.** Semiconductor heterostructures, in which quantum Hall-effect is observable.

Heterostructures (well/barrier)	Difference in electronegativity of constituent atoms of the well	Effective mass ( $m^*/m_0$ )	Mobility [ $10^4 \text{ cm}^2/\text{Vs}$ ]	Carrier re- laxation time ( $\tau/\tau_{\text{Si}}$ )	Ref.
Si/SiO <sub>2</sub>	0	0.19 (electron)	1.2	1	6
SiGe/Si	0	0.30 (hole)	0.33	0.43	7
HgTe/CdTe	0.2	0.025 (electron)	5.3	0.58	8
InGaAs/InP	0.35	0.047 (electron)	5.1	1.1	9
GaAs/AlGaAs	0.4	0.067 (electron)	7.9	2.3	10
GaN/AlGaN	1.4	0.22 (electron)	1.05	1	11
ZnO/MgZnO	1.9	0.32 (electron)	0.55	0.77	12

**Table II.** Growth and electronic parameters of ZnO/Mg<sub>x</sub>Zn<sub>1-x</sub>O heterostructures.

sample	Thickness of ZnO ( $\mu\text{m}$ )	Growth Temp. ( $^{\circ}\text{C}$ )	Mg con- tent $x$	Electron density ( $10^{12} \text{ cm}^{-2}$ )		Mobility [ $\text{cm}^2/\text{Vs}$ ]	
				1 K	300 K	1 K	300 K
A	1.1	1020	0.15	0.66	39	5500	150
B	0.4	900	0.20	1.8	5.0	4900	160
C	0.4	1000	0.20	3.7	11	2700	160

**Table III.** Reported experimental lattice parameters of various wurtzite crystals.

Substance	$a^*$	$c^*$	$(a/c)^2$	$u$	Ref.
2H-SiC	3.079	5.053	0.3713	0.3760	64
CdSe	4.299	7.010	0.3761	0.3768	64
GaN	3.189	5.185	0.3783	0.377	63
CdS	4.136	6.713	0.3796	0.3788	60
BeO	2.698	4.379	0.3796	0.3775	64
ZnO	3.250	5.204	0.3900	0.3786	62
AlN	3.112	4.982	0.3902	0.3820	64
InN	3.540	5.705	0.3850	0.3825	61
				0.3821	63
				N.A.	

\*Widely accepted lattice constants are used.

**Table IV.** Reported theoretical lattice parameters of various wurtzite crystals.

Substance	$(a/c)^2$	$u$	$P_{\text{sp}}$ ( $\text{C}/\text{m}^2$ )	$e_{33}$ ( $\text{C}/\text{m}^2$ )	$e_{31}$ ( $\text{C}/\text{m}^2$ )	Ref.
ZnS	0.3727	0.3749		0.24		57
GaN	0.3747	0.376	-0.029	0.73	-0.49	58
	0.3782	0.379				67,68
	0.3782	0.377				66
	0.375	0.378				65
BeO	0.3815	0.379	-0.036	0.04	-0.72	59
	0.3768	0.3782				57

InN	0.3778	0.377	-0.032	0.97	-0.57	58
	0.3853	0.380				67,68
	0.3815	0.3784				66
	0.3834	0.380				65
ZnO	0.3906	0.383	-0.057	1.19	-0.53	59
	0.3897	0.3812	-0.05	0.92	-0.39	57
			-0.057	0.89	-0.51	58
	0.3858	0.378	-0.022			69
AlN	0.3859	0.378		1.34	-0.57	69
	0.3815	0.380	-0.081	1.46	-0.60	58
	0.3897	0.381				67,68
	0.3887	0.3814				66
MgO*	0.3848	0.381				65
	0.4328	0.395	-0.144			69
	0.3906	0.383	-0.06			69

\*Deformed crystal under biaxial strain. The in-plane lattice parameters  $a$  are constrained to some values, whereas  $(c/a)$  and  $u$  are unconstrained.

**Table V.** Peak mobility and critical carrier density  $n_c$  at metal-to-insulator transitions in ZnO/Mg<sub>x</sub>Zn<sub>1-x</sub>O interfaces.

Growth technique	Method	Temperature	Peak mobility [cm <sup>2</sup> /Vs]	$n_c$ [cm <sup>-2</sup> ]	Ref.
PLD	Photo-excitation	4 K	3000	$6 \times 10^{11}$	91
PLD	Field effect (MIS)	2 K	5000	$6 \times 10^{11}$	92
MBE	Field effect (MES)	2 K	21000	$1 \times 10^{11}$	90

## Figure Captions

**Fig. 1.** Schematic structures of prototype ZnO based transistors. (a) bottom gate and polycrystalline channel, (b) top gate and epitaxial channel, (c) top gate with lattice-matched  $\text{Mg}_x\text{Ca}_{1-x}\text{O}$  dielectric layer and epitaxial channel on  $\text{Mg}_x\text{Zn}_{1-x}\text{O}$  buffer layer. (d) Progress made over the years in room-temperature mobility of ZnO heteroepitaxial films (open circles), field-effect transistors with polycrystalline channels (triangles) and epitaxial channels (stars). Note that data obtained for the devices shown in (a) to (c) are highlighted. Some milestones are shown by inset pictures.

**Fig. 2.** (a) Photograph of a  $\text{ScAlMgO}_4$  single crystal (measure scale in cm). The top flat surface is crystallographic (0001) plane. (b) Schematic illustration of the (0001) heterointerface between ZnO and  $\text{ScAlMgO}_4$  projected along the  $[11\bar{2}0]$  direction.

**Fig. 3.** Hall mobility as a function of gate electric field [or sheet carrier density ( $-1/R_{\text{H}}e$ )] of the carriers accumulated at the ZnO/ $\text{ScAlMgO}_4$  interface. The inset depicts structure of the field-effect transistor.

**Fig. 4.** AFM images and height profiles of (a) as-grown and (b) annealed ZnO films on the (0001) sapphire substrate. The same set for (c) as-grown and (b) annealed ZnO films on the (0001)  $\text{ScAlMgO}_4$  substrates. Scale bar,  $1 \mu\text{m}$ , shown in (d) is common for all the images.

**Fig. 5.** (a-e) AFM images of the films grown on HITAB layers. Scale bar,  $1 \mu\text{m}$ , shown in (a) is common for all the images. (f) AFM image of the films grown directly on  $\text{ScAlMgO}_4$  substrate at  $1000^\circ\text{C}$ . Scale bar,  $2 \mu\text{m}$ . (g) Analyses of the AFM images from (a) to (f). Surface fraction of different terrace levels, represented by different size dots, is plotted as a function of growth temperature.

**Fig. 6.** Progress made over the years in free carrier density ( $n$ ) and Hall mobility ( $\mu_{\text{H}}$ ) of ZnO heteroepitaxial films ( $\bullet$ ). ‘Bulk’ represents characteristics of bulk samples grown by vapor-phase transport technique ( $\circ$ ).

**Fig. 7.** (a) Photograph of a pulsed-laser deposition system. (b) Schematic illustration of system components and a substrate holder used for temperature-gradient

epitaxy method.

**Fig. 8.** (a) Optical microscope image of a micro-patterned Hall-bar array (sample mounted on a chip carrier). (b) Optical microscope image of a Hall-bar device made of transparent ZnO film and ScAlMgO<sub>4</sub> substrate, and opaque metal electrodes.

**Fig. 9.** Growth temperature dependence of carrier density  $n$  (a) and Hall mobility  $\mu_H$  (b) at 300 K. The ZnO films were grown on semi-insulating Mg<sub>0.15</sub>Zn<sub>0.85</sub>O HITAB layers in  $P_{O_2}$  of  $1 \times 10^{-6}$  Torr (●) and  $1 \times 10^{-7}$  Torr (▲).

**Fig. 10.** AFM images of (a) a Mg<sub>0.15</sub>Zn<sub>0.85</sub>O HITAB layer and (b) a ZnO layer grown on the HITAB layer. (c) HRXRD pattern of a ZnO/Mg<sub>0.15</sub>Zn<sub>0.85</sub>O heterostructure (solid line) and simulated curve (dotted line).

**Fig. 11.** Magnetic field dependence of the transverse ( $\rho_{xx}$ ) and longitudinal ( $\rho_{xy}$ ) magnetoresistivity of the ZnO/Mg<sub>x</sub>Zn<sub>1-x</sub>O heterostructures having different carrier densities ( $0.66, 1.8, \text{ and } 3.7 \times 10^{12} \text{ cm}^{-2}$  for sample a, b, and c, respectively). The Landau filling indices ( $\nu$ ) are identified by the horizontal bars and numbers

**Fig. 12.** Estimation of spontaneous polarization in Mg<sub>x</sub>Zn<sub>1-x</sub>O. (a, b) The internal parameters  $u$  versus  $(a/c)^2$  in various wurtzite crystals, (a) experimental and (b) theoretical data, listed in Table III and IV, respectively. The dotted lines represents ideal wurtzite lattice expressed by a simple equation  $u = \frac{1}{3}(a/c)^2 + \frac{1}{4}$ . (c) Plots of  $P_{sp}$  (to right ordinate) and piezoelectric constants (to left ordinate) versus  $u$ , made from the theoretical data (Table IV). Closed circles and triangles are  $P_{sp}$  values calculated by first-principle computations and point-charge model, respectively. The shaded region represents the standard deviations of the least squares fit to the first-principle data. (d)  $P_{sp}$  versus  $x$  in Mg<sub>x</sub>Zn<sub>1-x</sub>O obtained in a combination of (a) with (c).

**Fig. 13.** (a) Schematic of the ZnO/Mg<sub>x</sub>Zn<sub>1-x</sub>O heterostructures grown on ScAlMgO<sub>4</sub> substrates. Depending on the sign of  $|\Delta P_{sp}(x)| - |P_{pe}(x)|$ , an accumulation layer represented by broken lines is formed either at the surface or in the interface. (b) Calculated (shaded region surrounded by dotted lines) and measured (closed circles)  $n$  as a function of Mg content  $x$  in the barrier. Shaded region surrounded by solid lines  $[|P_{pe}(x)/e|]$  and solid curve  $[|\Delta P_{sp}(x)/e|]$  were calcu-

lated by using theoretical values listed in Table IV.

**Fig. 14.**  $\Delta P_{\text{sp}}(x)$  reported by us and Malashevich *et al.* (Ref. 70)

**Fig. 15.** (a) Band-gap as a function of oxide ion distance ( $a_{\text{RS}}/\sqrt{2}$ ) along the (111) plane of various rock-salt oxides. Vertical dotted line presents the  $a$ -axis lattice constant of ZnO. (b) Schematic illustration of atomic structure of  $\text{Mg}_x\text{Ca}_{1-x}\text{O}$ .

**Fig. 16.** X-ray diffraction reciprocal space maps for  $\text{Mg}_x\text{Ca}_{1-x}\text{O}/\text{ZnO}$  heterostructures grown on  $\text{ScAlMgO}_4$  substrates.

**Fig. 17.** (a) Output curves for various  $V_G$  and (b) transfer curves measured at room temperature for the device shown in Fig. 1 (c). For evaluation of  $\mu_{\text{FE}}$ ,  $I_d^{1/2}$  for saturation regime are given to right ordinates.

**Fig. 18.** Schematic of cross-sectional layer structures (left) and conduction band diagrams (right) for (a) a  $\text{ZnO}/\text{Mg}_x\text{Zn}_{1-x}\text{O}$  single heterostructures and (b) a double heterostructures with atomic-layer-deposited  $\text{a-AlO}_x$  gate dielectric.

**Fig. 19.** Field- and Hall-effect characteristics of the device at 2 K. (a) Output curves measured in a  $V_g$  range of -2 V to 8 V. The inset shows  $V_g$  dependence of  $\rho_{\text{xx}}$  and leakage current. (b) Hall mobility ( $\mu_{\text{H}}$ ) as a function of 2DEG density ( $n$ ) evaluated from Hall effect (closed circles). The 2DEG density evaluated from SdH oscillations is also plotted by open circles. Inset depicts  $V_g$  dependence of  $n$ . Straight line is a linear fit. Critical carrier density ( $n_c$ ) of the insulator-to-metal transition is  $\sim 6 \times 10^{11} \text{ cm}^{-2}$  (broken line).

**Fig. 20.** Temperature dependence of longitudinal resistivity  $\rho_{\text{xx}}$  measured in a  $V_g$  range of -2 V to 6 V with using a standard lock-in technique under ac excitation (12~20 nA, 19 Hz).

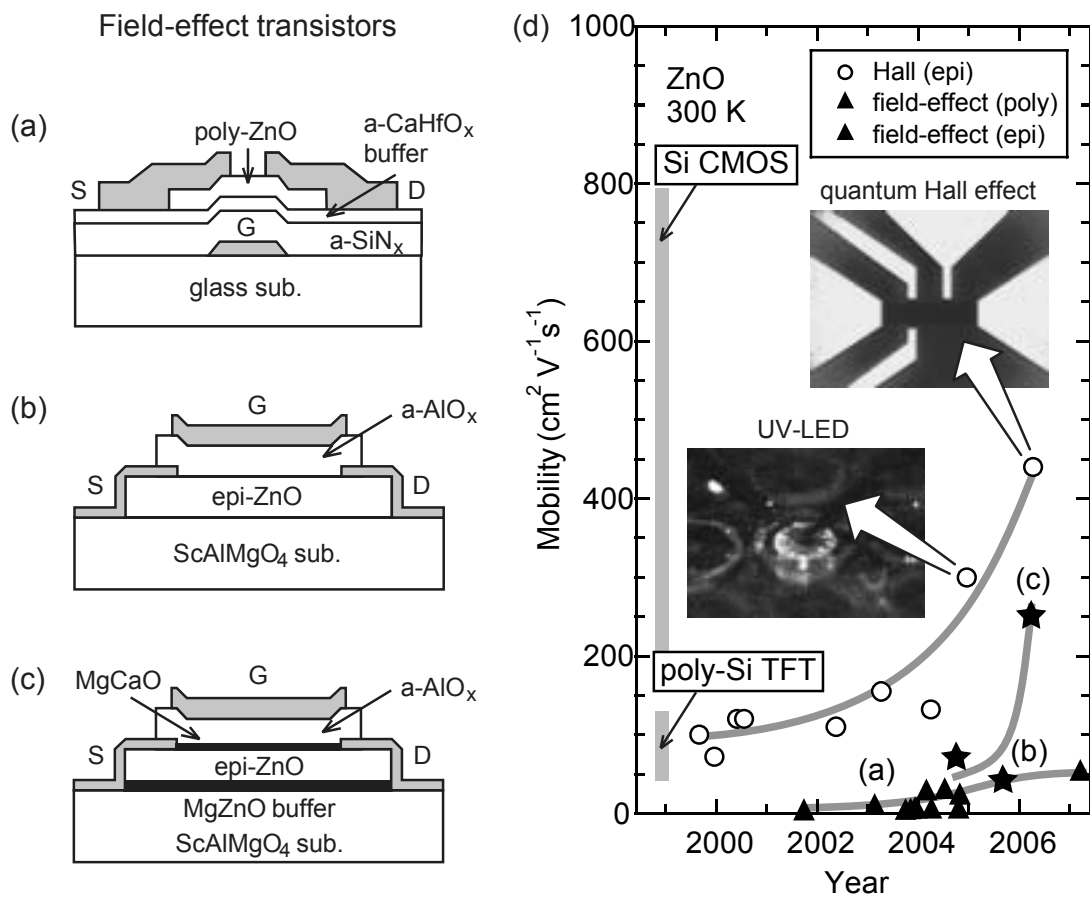


Fig. 1

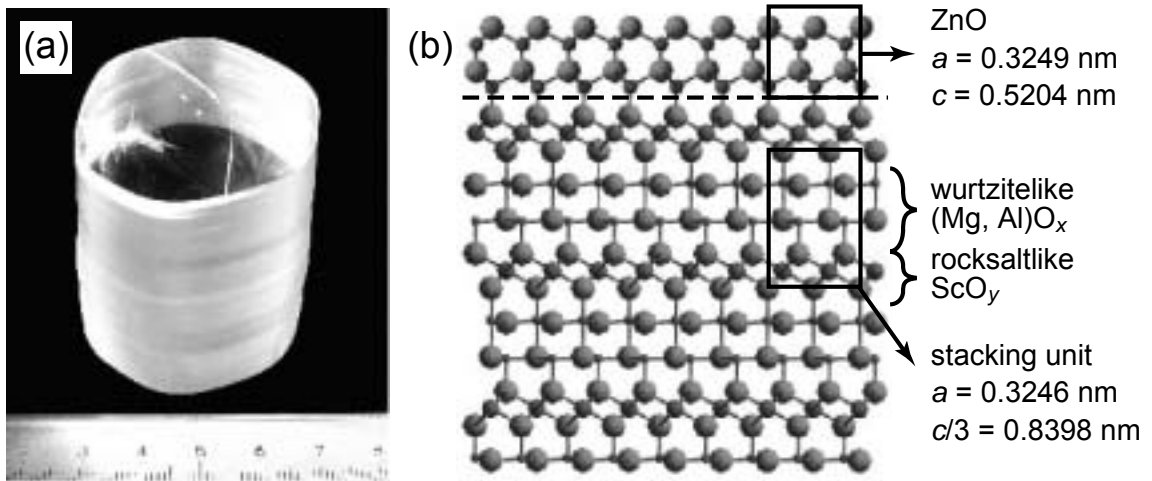


Fig. 2

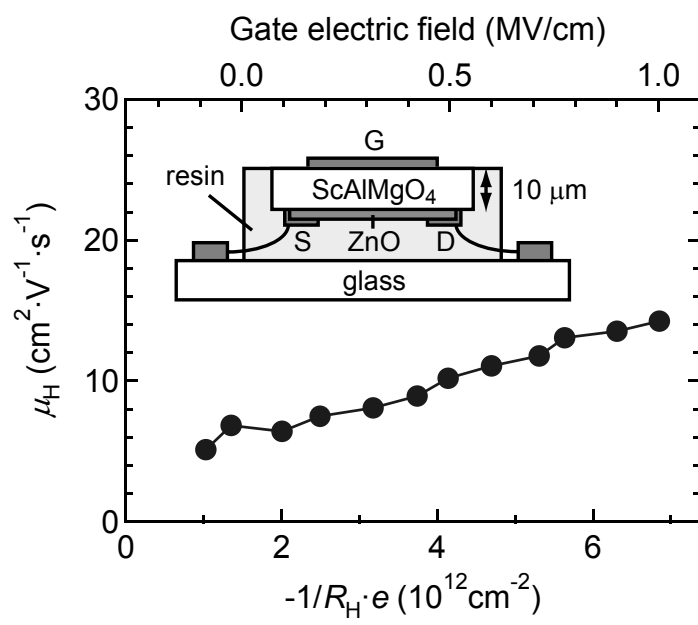


Fig. 3

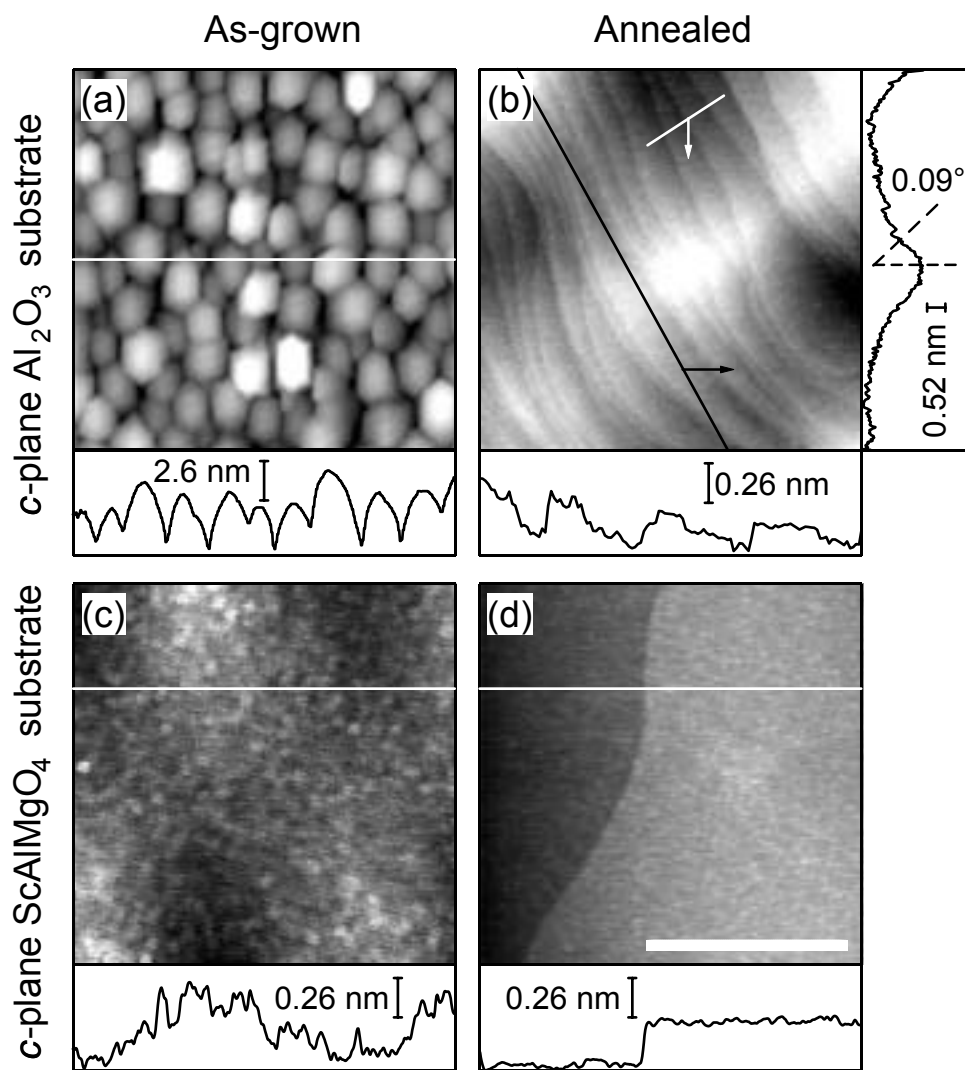
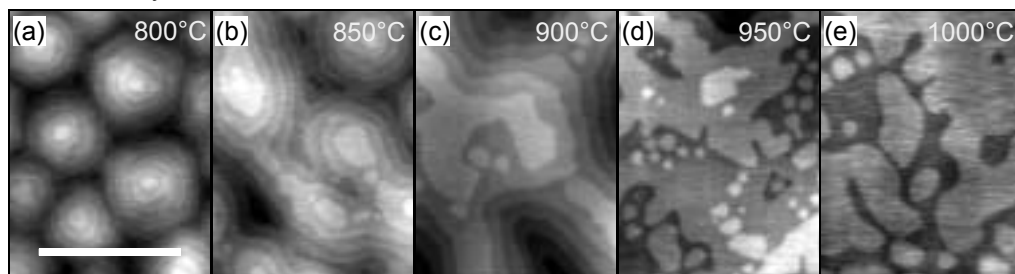


Fig. 4

on HITAB layer



No HITAB layer

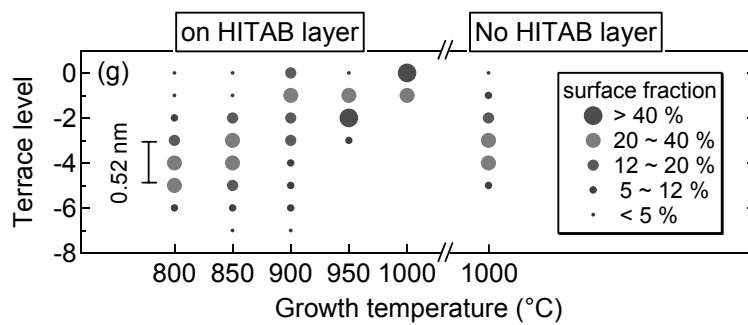
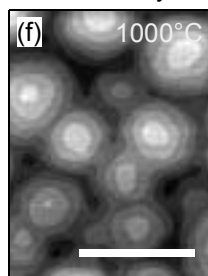


Fig. 5

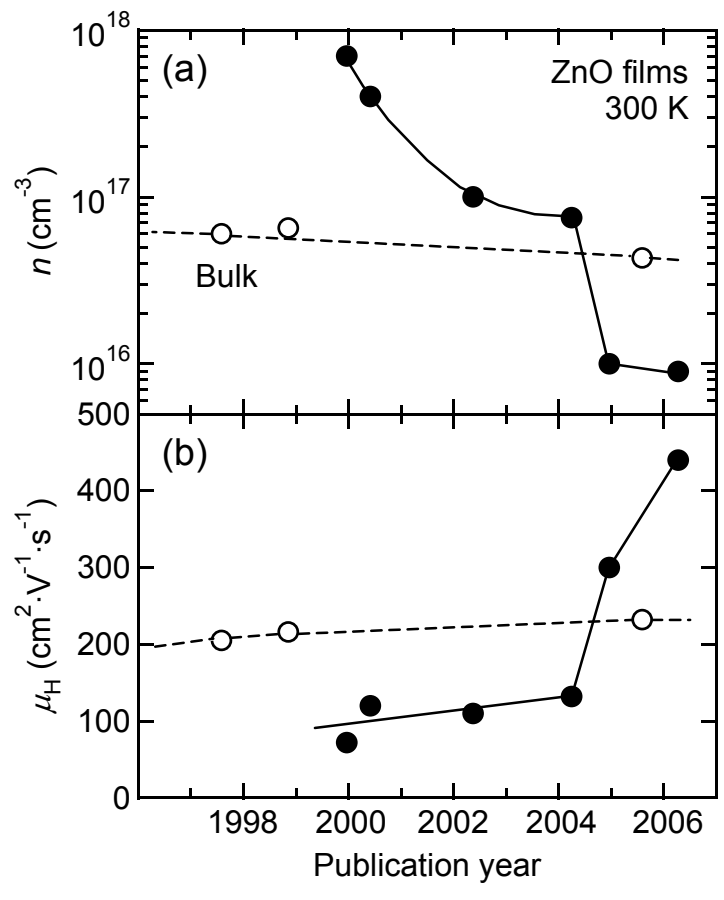


Fig. 6

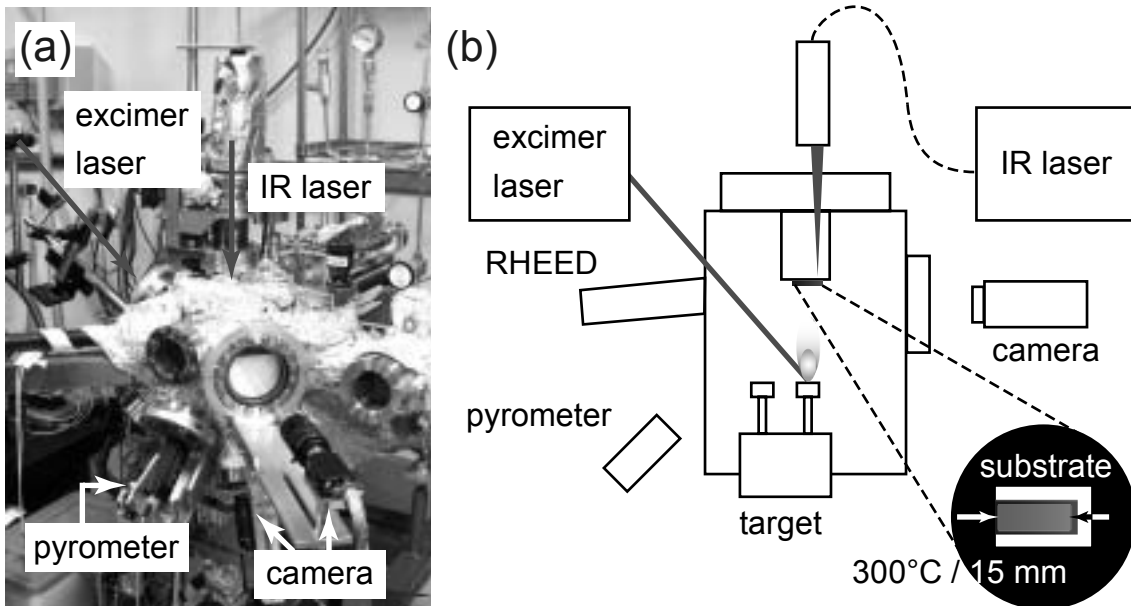


Fig. 7

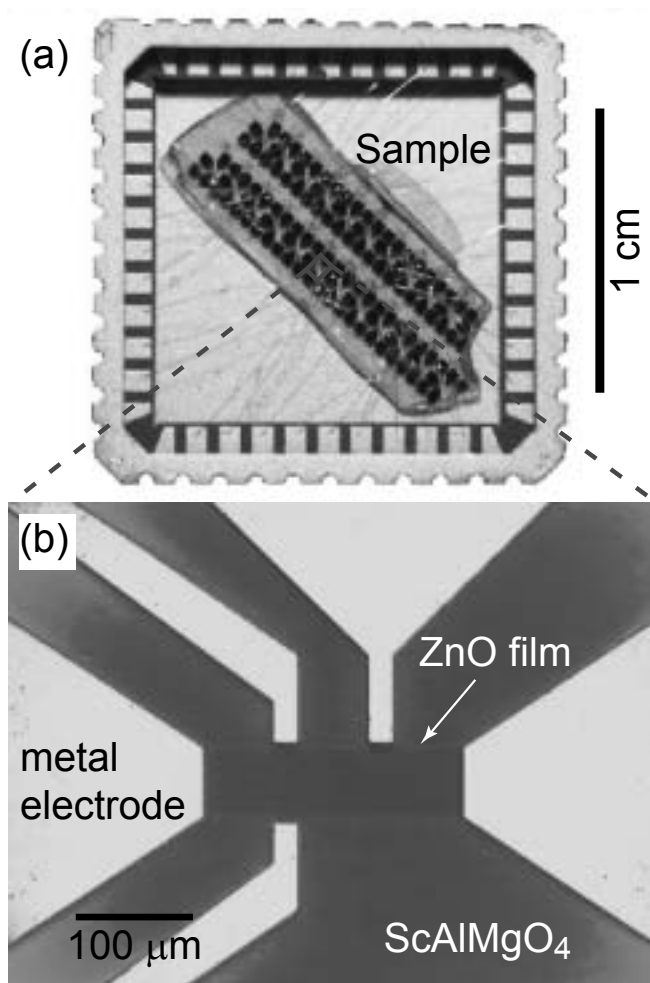


Fig. 8

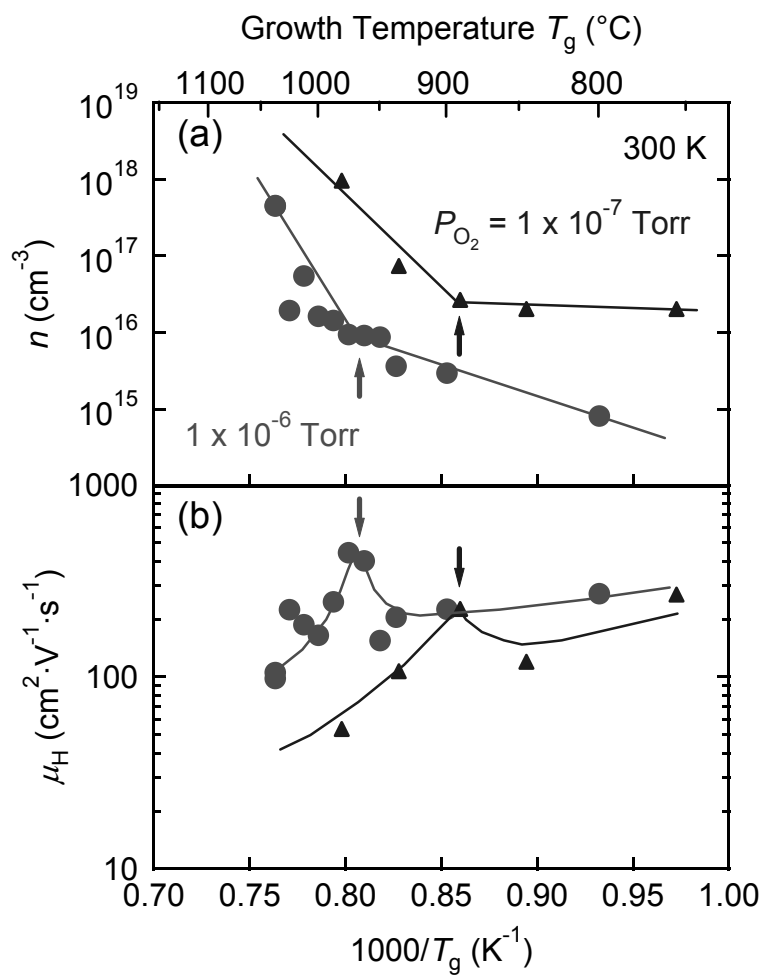


Fig. 9

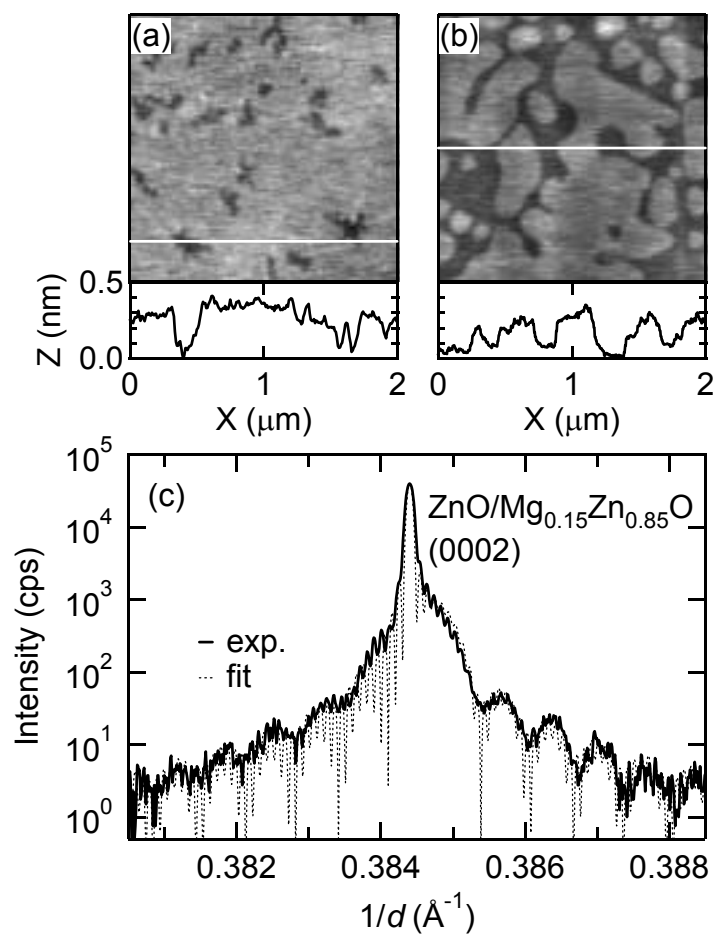


Fig. 10

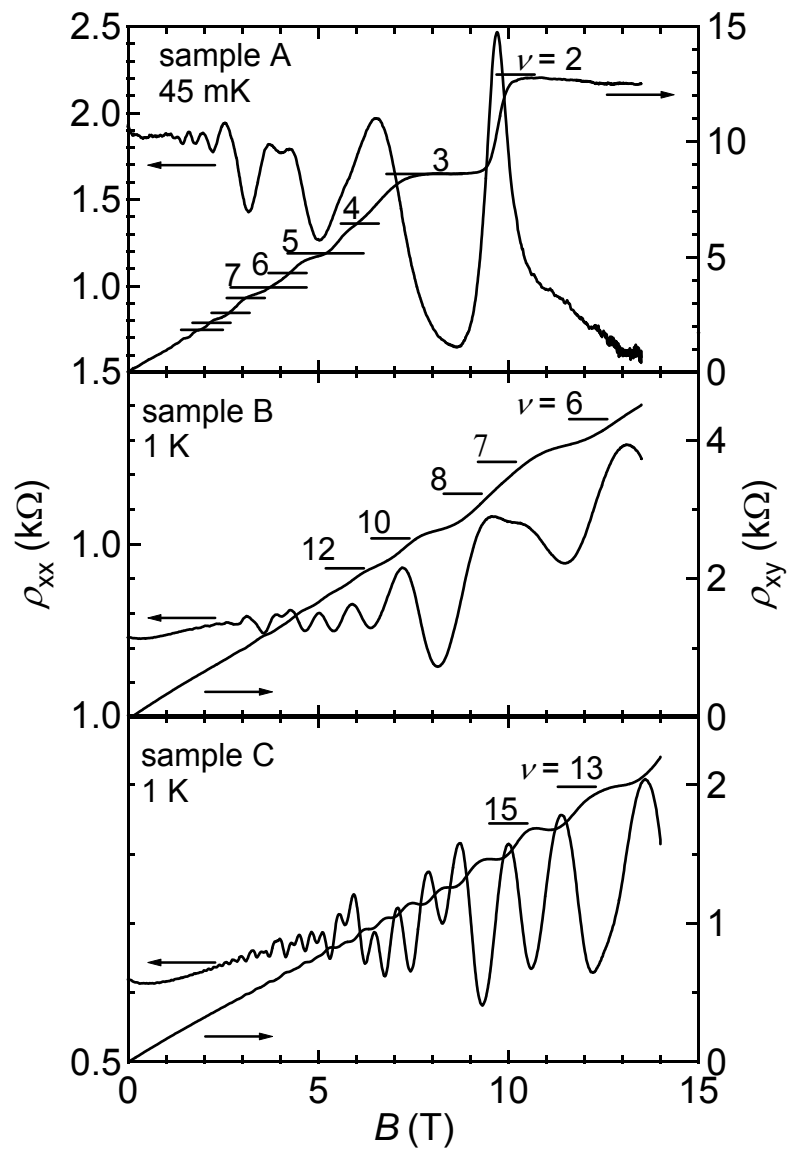


Fig. 11

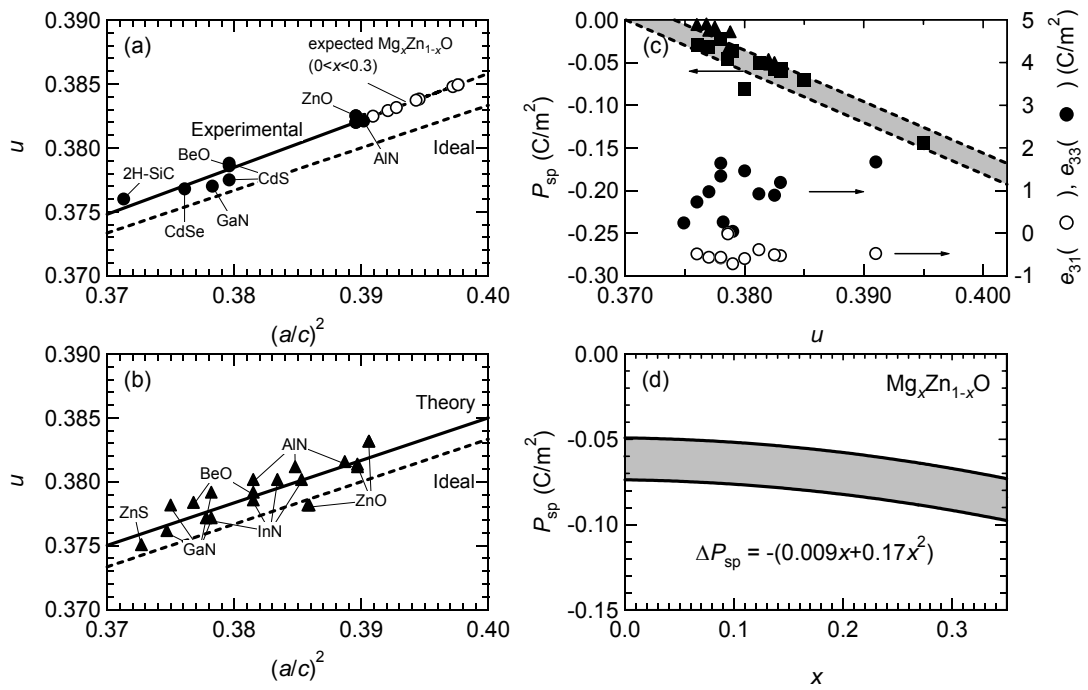


Fig. 12

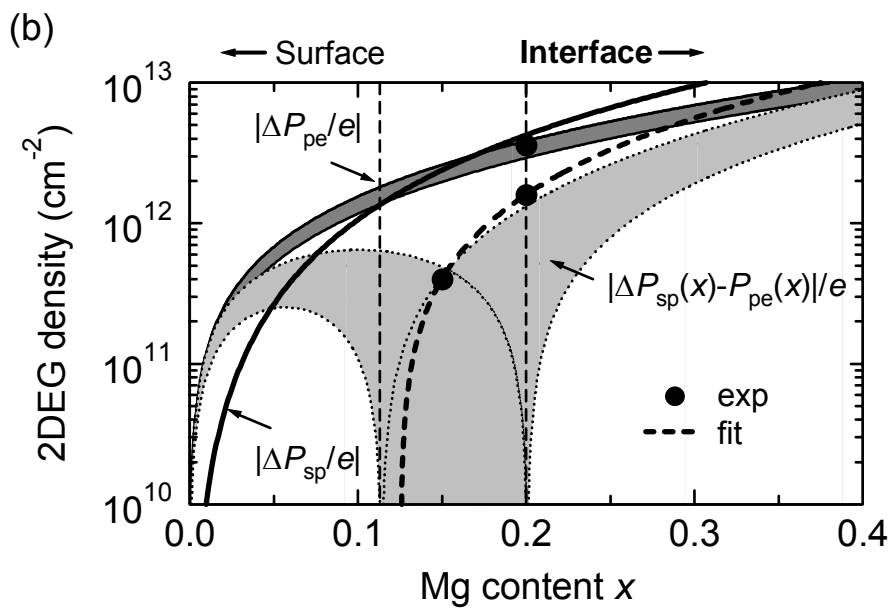
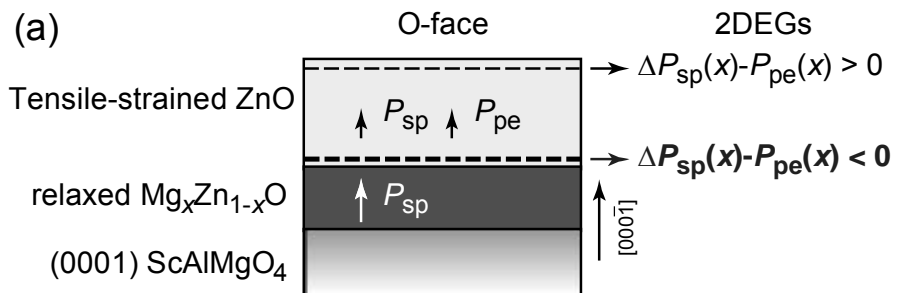


Fig. 13

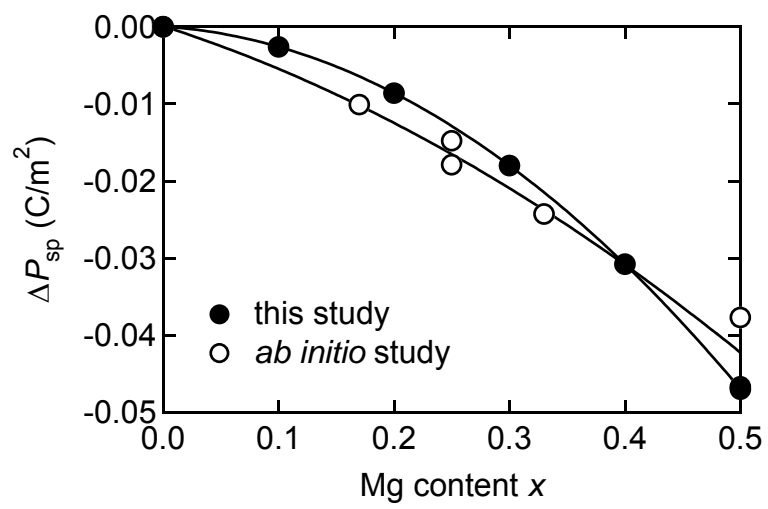


Fig. 14

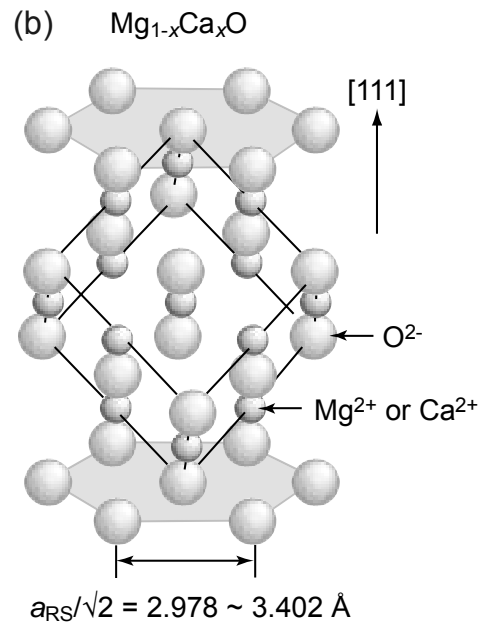
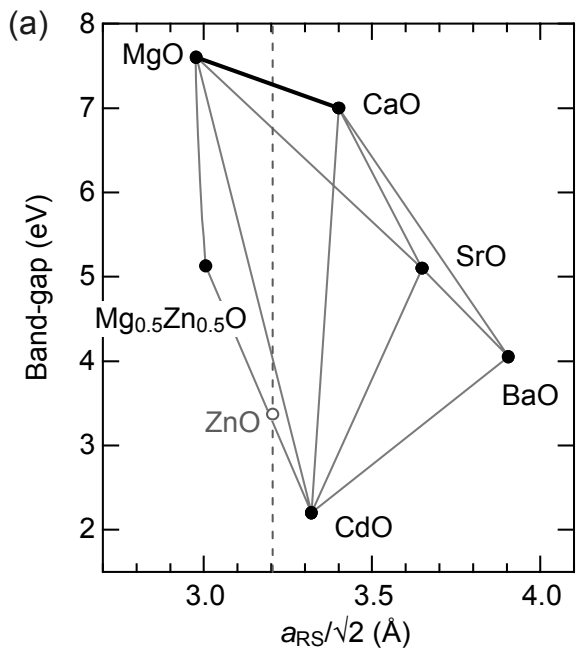


Fig. 15

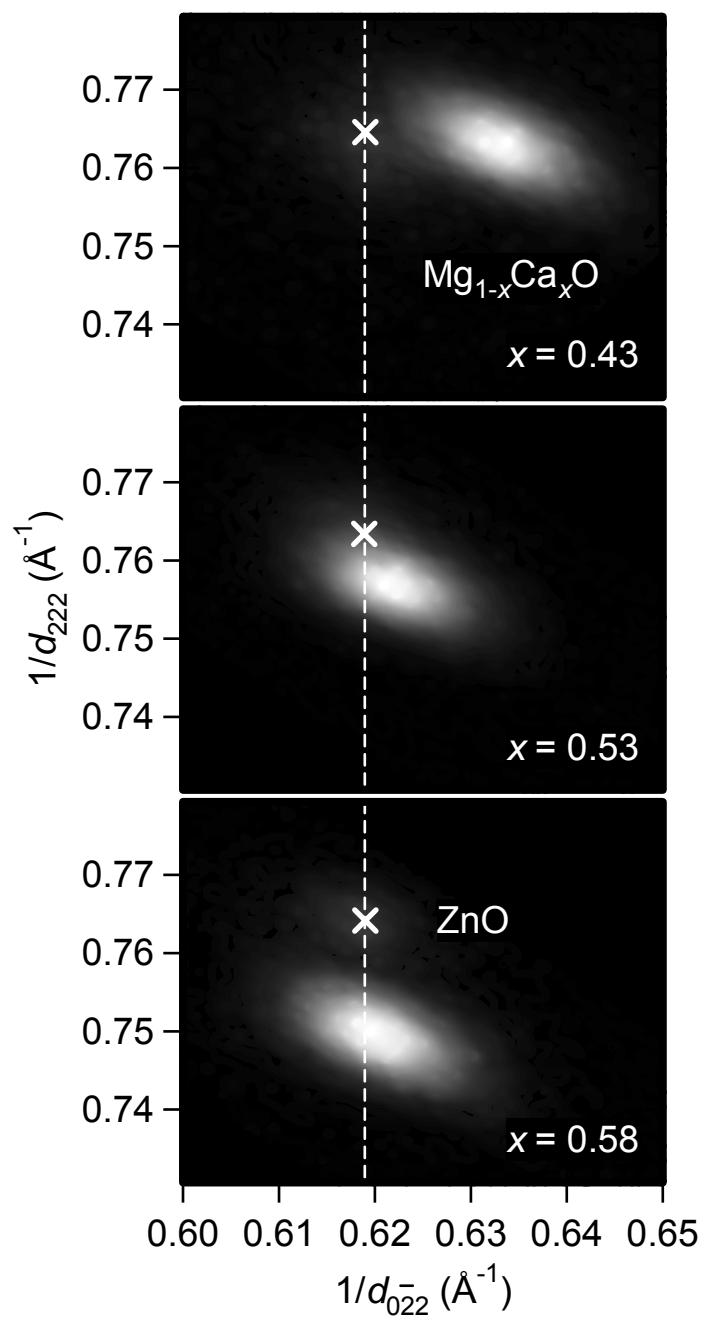


Fig. 16

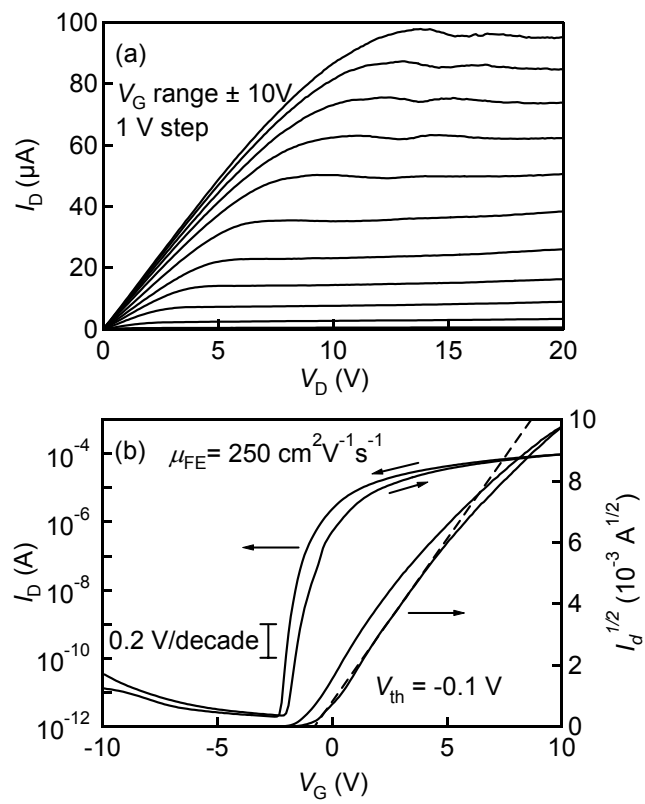


Fig. 17

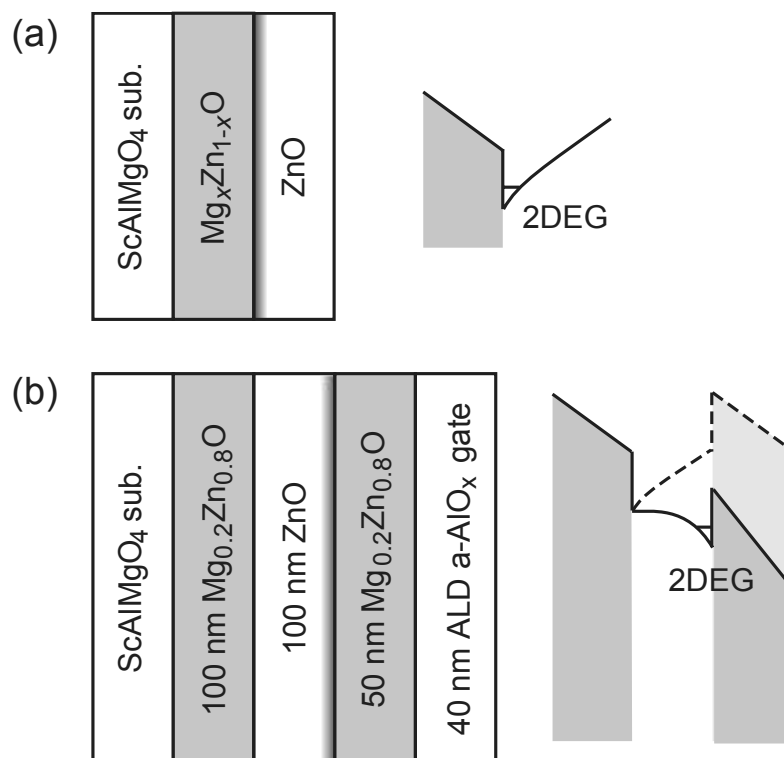


Fig. 18

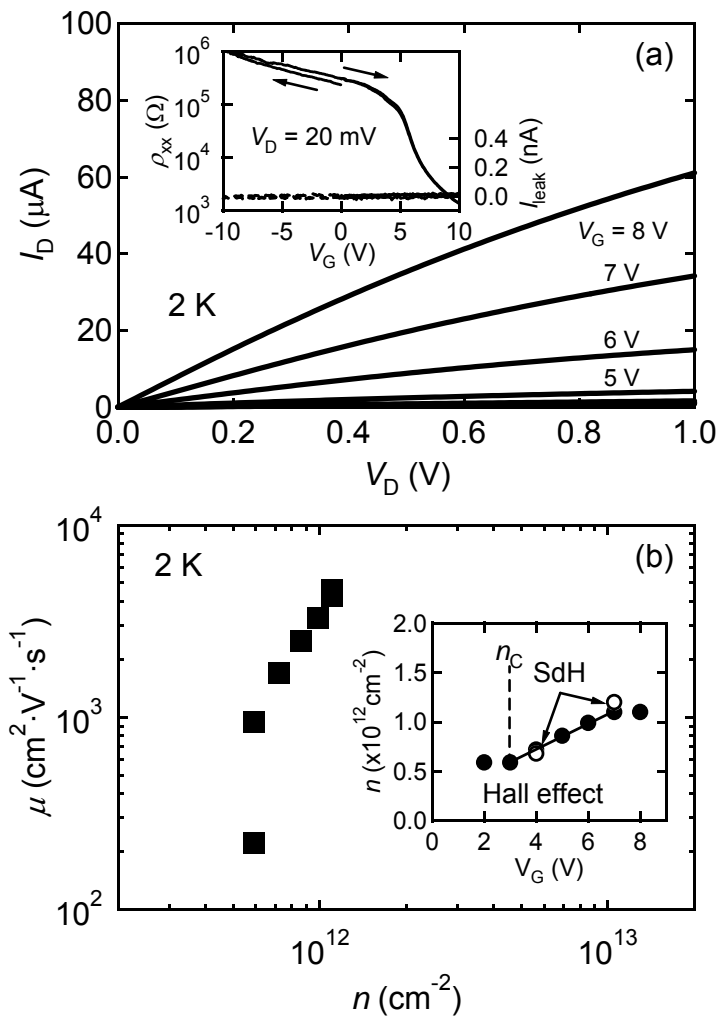


Fig. 19

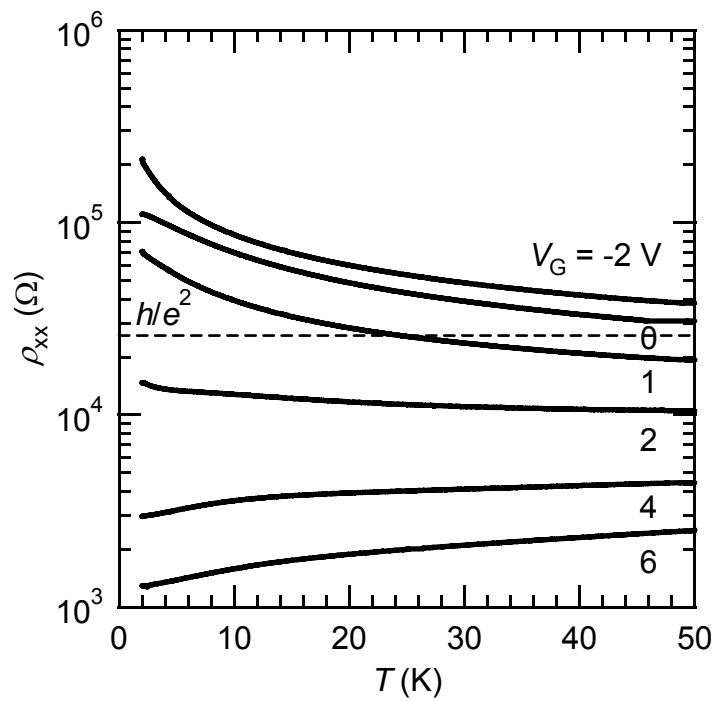


Fig. 20